Copyright

by

Feng Lu

2015

The Dissertation Committee for Feng Lu Certifies that this is the approved version of the following dissertation:

Infrared Nano-Spectroscopy via Molecular Expansion Force Detection

Committee:

Mikhail A. Belkin, Supervisor

Edward T. Yu

Ananth Dodabalapur

Gennady Shvets

Christopher J. Ellison

Infrared Nano-Spectroscopy via Molecular Expansion Force Detection

by

Feng Lu, B.S.; M.S.

Dissertation

Presented to the Faculty of the Graduate School of
The University of Texas at Austin
in Partial Fulfillment
of the Requirements
for the Degree of

DOCTOR OF PHILOSOPHY

The University of Texas at Austin
December 2015

Dedication

To my parents.

Acknowledgements

The past six and half years at UT Austin have been a very important time period to me. I consider myself very lucky to have worked with a group of people who are very talented and nice. Without the support from them, the work in this dissertation would not have been completed.

I couldn’t find a proper word to sufficiently describe my gratitude to my supervisor, Prof. Mikhail A. Belkin. He is an amazing scientist and a fatherly mentor. His never ending scientific curiosity and skepticism, his ability to provide clear physical pictures, and his “Russian-style” creativity and resolution to make things work are among many of his characteristics that I admire and will try to learn throughout my career. From day one, he has been teaching me hand over hand from theories to experimental skills, from paper writing to presentation, in a very patient and encouraging way. The Ph.D. training he gifted to me is a fortune of my life.

I would like to thank Prof. Edward T. Yu, Prof. Ananth Dodabalapur, Prof. Gennady Shvets, Prof. Christopher J. Ellison, and Prof. Stanislav Emelianov for serving on my qualifying examination committee and dissertation committee. The collaboration with Prof. Shvets and his group on the chiral metasurface project is a learningful and pleasant experience.

My thanks also go to the past and present members of Belkin group. Robert Adams and Min Jang are the first two fellow graduate students I met in the lab. Robert is knowledgeable about mechanics and his DIY spirit influenced me. Min taught me nanofabrication skills. His samples, tools and lab notes were always handled elaborately, which is impressive. Jongwon Lee joined the group shortly after me. He carried out many research projects efficiently and has clear thought about his career. I was lucky to participate in some of his work. Each group has a witty man, and Karun Vijayraghavan is the one in our lab. His optimism infects the team and it is truly enjoyable to talk and hangout with him. Aiting Jiang is a master of nanofabrication, from whom I learned a lot. Mingzhou Jin worked with me on some projects in this dissertation and she is now pushing our technique to the next step. It is a wonderful experience to work with Dr. Seungyong Jung, who is very resourceful in semiconductor lasers and very considerate. I would also like to thank other lab fellows: Dr. David Austin, Yifan Jiang, Jaehyun Kim, Nishant Nookala and Yingnan Liu.

The work in this dissertation got generous support and advice from many colleagues in other institutions. Georg Ramer from Vienna University of Technology is a very enthusiastic researcher and Labview master. He helped to build our first fast spectrum acquisition system which was originally developed in his group led by Prof. Bernhard Lendl. I also give my thanks to Dr. Craig Prater and Kevin Kjoller at Anasys Instruments, Inc., to Prof. Vladislav V. Yakovlev at Texas A&M University and to Prof. François Lagugné-Labarthet at the University of Western Ontario.

Last but not least, I am deeply grateful to my parents, whom I can never repay for their selfless love and support.

Infrared Nano-Spectroscopy via Molecular Expansion Force Detection

Feng Lu, Ph.D.
The University of Texas at Austin, 2015

Supervisor: Mikhail A. Belkin

Mid-infrared absorption spectroscopy in the "molecular fingerprint" region (λ = 2.5–15 μm) is widely used for in situ analysis of chemical and biological samples. Due to the diffraction limit, traditional far-field techniques such as Fourier-transform infrared spectroscopy cannot take sample spectra with nanometer spatial resolution. To conduct nanoscale infrared measurement, in photoexpansion nano-spectroscopy, an atomic force microscope cantilever is used as a light absorption detector, in the way that the cantilever is deflected proportionally by the localized sample heating and expansion induced by infrared pulses. Previous studies of this new opto-mechanical technique demonstrated its powerfulness and simplicity, but relied on using high-power laser pulses to produce detectable cantilever deflection signal and it was difficult to measure ultra-thin samples below ~100 nm. In addition, the spatial resolution, though improved, is limited by the thermal diffusion length inside samples.

This dissertation presents a set of experiments which have substantially improved photoexpansion nano-spectroscopy in terms of sensitivity and spatial resolution, and have explored other aspects of this technique. For the first time, high-quality photoexpansion spectra have been obtained from molecular monolayers using low-power infrared pulses from a tunable quantum cascade laser. The orders of magnitude improvement in sensitivity is due to the two methods we implemented: mechanical enhancement by the cantilever resonance, and optical enhancement by the metalized cantilever tip. The spatial resolution is also improved and now only determined by the locally enhanced field below the tip. After that, the dissertation shows the spectral background signal, which comes from infrared absorption by the substrate and tip, can be suppressed using a second laser. We have also investigated the nonlinearity of tip-sample interaction, and are able to detect sample photoexpansion force at the heterodyne frequency. In the last part of this dissertation, we use our technique to image local optical energy distribution and ohmic heat dissipation of the metal nanoantennas.

Table of Contents

List of Tables xi

List of Figures xii

Chapter 1 Overview: Vibrational Nano-Spectroscopy 1
- 1.1 Molecular vibration and fingerprint 1
- 1.2 Vibrational spectroscopy 3
- 1.3 Current nano-spectroscopy techniques 6
- 1.4 Dissertation overview 8

Chapter 2 AFM Basics for Photoexpanison Measurement 10
- 2.1 Introduction 10
- 2.2 Origin of photoexpansion force 11
- 2.3 Detection and calibration of cantilever deflection 13
- 2.4 Cantilever bending modes 15
- 2.5 Cantilever thermal noise 23

Chapter 3 Cantilever Resonance Enhanced IR Nano-Spectroscopy with QCL ...24
- 3.1 Introduction 24
- 3.2 Prototype of photoexpansion nano-spectroscopy 25
- 3.3 Theory of cantilever resonance enhancement 27
- 3.4 Experiment 31
- 3.5 Results and discussion 34
- 3.6 Conclusion 40

Chapter 4 Tip-Enhanced IR Nano-Spectroscopy on Molecular Monolayer 41
- 4.1 Introduction 41
- 4.2 Tip enhancement in mid-IR 42
- 4.3 Monolayer photoexpansion 45
- 4.4 Experiment 48
- 4.5 Results and discussion 53
- 4.6 Conclusion 61

Chapter 5 Photoexpansion Background Suppression with Two QCLs 62
5.1 Introduction 62
5.2 Experiment 63
5.3 Results and discussion 65
5.4 Conclusion 69

Chapter 6 Heterodyne Detection of Photoexpanison Force 70
6.1 Introduction 70
6.2 Theory 71
6.3 Experiment 73
6.4 Conclusion 77

Chapter 7 Characterization of Plasmonic Metasurface 78
7.1 Introduction 78
7.2 Experiment 79
7.3 Conclusion 86

Chapter 8 Conclusion 87

Bibliography 89

List of Tables

Table 4.1: Material parameters for simulating tip enhancement and monolayer heating. 45

List of Figures

Figure 1.1: Vibrational energy level diagram for an asymmetric diatomic molecule at the ground electronic state, with the transitions via IR absorption (red arrow) and Raman scattering (purple arrow) illustrated. 2

Figure 2.1: **(a)** Mechanism of AFM cantilever deflection during sample photoexpansion. Blue solid curve shows the dependence of the interaction force between the sample surface and the AFM cantilever tip on tip-surface distance (z). Red dashed curve is shifted along z-axis by sample photoexpansion $\Delta\delta$. F_T is the photoexpansion force acting on the AFM cantilever; z_0 is the position of the AFM cantilever in contact mode. The figure is not drawn to scale. **(b)** Illustration of contact between a tip and an elastic sample plane. The repulsive tip-sample force is generated by the sample indentation δ. 11

Figure 2.2: Schematic of AFM configuration. The cantilever deflection is measured by an optical level system which is composed of a visible laser beam and a position sensitive photodetector (PSPD). 13

Figure 2.3: Cantilever resonances in free space. **(a)** Cantilever shape for the first three bending modes calcualted using Eqs. (2.5) and (2.7). The corresponding eigenfrequencies are calcualted using Eq. (2.8) for a ContGB-G cantilever. **(b)** Measured noise spectrum of that cantilever. 17

Figure 2.4: Cantilever resonances when in contact with the sample. **(a)** The vertical and lateral tip-sample interactions are approximated with the effective spring constants $k*$ and $k*_{Lateral}$. **(b)** Cantilever shape for the first three bending modes when k^*/k_1=1,000, calcualted using Eqs (2.5) and (2.10). 19

Figure 2.5: AFM Force-distance curve measured on a 300 nm-thick PMMA film. Sample adhesion force $F_{pull-off}$ and contact mode setpoint force $F_{setpoint}$ are compared. 21

Figure 2.6: Comparing the cantilever deflection amplitude between the first bending mode in free space (black) and second bending mode in contact with the sample (red), with the same PSPD output voltage (slope of the tip end). 22

Figure 3.1: Setup and signal extraction in prototype photoexpansion nano-spectroscopy. **(a)** Schematic setup. **(b)** Recorded cantilever ring-down oscillation induced by one mid-IR pulse. **(c)** Corresponding frequency domain signal by applying Fourier transform on (b). **(d)** Absorption spectrum obtained via tuning the laser wavelength. This set of figures was acquired from Anasys Instruments. 26

Figure 3.2: Comparing cantilever oscillation at the second bending mode at 200 kHz excited by **(a)** 1 kHz pulses (off resonance) and **(b)** 200 kHz pulses (on resonance). 30

Figure 3.3: External-cavity quantum cascade laser (EC-QCL). **(a)** Schematic of the wavelength tuning mechanism. The external cavity is formed by a diffraction grating and the laser chip. **(b)** A commercial EC-QCL from Daylight Solutions, with its dimension compared to a US quarter. This set of figures was acquired from Daylight Solutions. 31

Figure 3.4: Power spectra of two commercial EC-QCLs available in the lab (from Daylight Solutions). MIRcat (blue) has four different QCL chips integrated. 32

Figure 3.5: Schematic of experimental setup for cantilever resonance enhanced photoexpansion spectroscopy using a tunable mid-IR QCL............34

Figure 3.6: The photoexpansion signal recorded as a function of the QCL pulse repetition frequency. 35

Figure 3.7: Comparing photoexpansion spectra of SU-8 (black) and LOR (red) obtained when the cantilever was on (solid curves) and away from (dotted curves) the cantilever mechanical resonance. Square data points and solid curves are the photoexpansion spectra obtained with the laser repetition frequency set at the AFM cantilever second bending mode of 155 kHz. Dashed curves are the reference absorption spectra measured by FTIR. Dotted curves near zero-level are the photoexpansion spectra obtained with the laser repetition frequency set at 130 kHz, which are also zoomed-in in the inset. 36

Figure 3.8: **(a)** The AFM topographic image of the 50-nm-thick SU-8 pattern of a Texas Longhorn on top of a 70-nm-thick LOR film on an undoped silicon substrate. Inset: the zoom-in image of the section of the SU-8 pattern with four points marking the positions at which the photoexpansion spectra shown in (b-e) are taken. The separation between the adjacent points is 50 nm. **(b-e)** Photoexpansion spectra (squares are data points, solid lines are for eye guiding) obtained at four sample points shown in (a). Dashed lines are FTIR absorption spectra of SU-8 (b,c) and LOR (d,e). **(f)** Photoexpansion image of Texas Longhorn pattern in (a) taken at laser wavelength of 1204 cm^{-1}. The image size is 128 by 128 pixels, each pixel correspond to a 50-nm-by-50-nm square. 37

Figure 3.9: Simulations of the temperature distribution in inhomogeneous polymer samples before, during, and after a single laser pulse. The samples are assumed to be illuminated by a 100 mW 40 ns-square pulse, focused to a 100 μm-radius area. **(a)** Temperature distribution at the very end of a laser pulse in a sample consisting of a SU-8 block (300 nm wide and 300 nm thick) placed on top of a 300-nm-thick layer of LOR on a silicon substrate. **(b)** Temperature variation along the dashed line in (a) before (0 ns), during (10 ns), and after (40 ns, 200 ns, and 5 μs) the laser pulse. **(c)** Temperature distribution at the very end of a laser pulse in a sample consisting of a SU-8 block (300 nm wide and 300 nm thick) embedded within a 300-nm-thick layer of LOR on a silicon substrate. **(d)** Temperature variation along the dashed line in (c) before (0 ns), during (10 ns), and after (40 ns, 200 ns, and 5 μs) the laser pulse. 39

Figure 4.1: Simulation of gold tip enhancement in the mid-IR region. **(a)** Local intensity distribution around the tip at $\lambda = 8$ µm. The cone-shaped tip is 10 µm long and light is incident at 75^{o} with respect to the tip axis. Simulation is performed with COMSOL in 3D. **(b)** Enhancement factor (I/I_0) as a function of wavelength. The values in (b) are extracted at the position10 nm below the tip apex. 43

Figure 4.2: Simulation of tip enhancement in a 2-nm gap formed by the gold tip and the gold substrate at $\lambda = 8$ µm. **(a)** The gap is filled with air. **(b)** The gap is filled with an organic monolayer with the refractive index of 1.5 + i0.38. The inset of (b) is a SEM image of an actual tip used in the experiment. The modeling parameters for the tip and incident light are the same as those in Fig. 4.1. 44

Figure 4.3: Simulation of monolayer sample heating. **(a)** Temperature increase at the end of a 160 ns-long pulse in and around a monolayer sample below the AFM tip. The monolayer is assumed to have an absorption coefficient $\alpha_{\text{th}} = 6{,}000$ cm^{-1} which corresponds to absorption in PEG and EG6-OH molecules at 1342 cm^{-1} (will be discussed in section 4.4). **(b)** Temperature variation along the blue dash line in (a) during (13 ns, 160 ns) and after (180 ns, 5 µs) the pulse. The sample is cooled to the room temperature before the next pulse arrives (assuming the repetition frequency of laser pulses is 200 kHz)...46

Figure 4.4: Simulation of monolayer sample expansion. **(a)** Dependence of tip-sample distance change $\Delta\delta$ due to sample expansion caused by a mid-IR pulse. **(b)** Histograms showing the accumulated sample expansion from the monolayer, substrate and tip for $\alpha_{abs} = 0$ cm^{-1} (left) and $\alpha_{abs} = 6{,}000$ cm^{-1} (right). The incident IR pulse was assumed to have a peak power of 500 mW and to be focused to a 100-μm-radius spot for the simulations, similar to the experimental situation. 47

Figure 4.5: Fabrication process of atomically flat template-stripped gold (TSG) substrate. 49

Figure 4.6: Topographic measurement of monolayer samples. **(a)** EG6-OH after partial O_2 plasma etching. The bright regions are EG6-OH monolayer while the dark regions are exposed gold. **(b)** Line-scan averaged within the red box in (a). **(c)** PEG monolayer islands self-assembled on gold after a short immersion time. Inset: line-scan along the blue line. ... 50

Figure 4.7: Schematic of the experimental setup for tip-enhanced photoexpansion nano-spectroscopy on monolayer detection. P-polarized light pulses from a mid-IR laser are focused on a sample. Cantilever deflection due to the molecular expansion force action is detected by a position-sensitive photodetector (PSPD). The PSPD signal is sent to the lock- in amplifier referenced by the laser pulse repetition frequency. The amplifier output is a measure of the cantilever oscillation amplitude at the lock-in reference frequency. 52

Figure 4.8: Molecular force spectra of self-assembled monolayers on gold. **(a)** EG6-OH. **(b)** NTP. The blue circles are the measured data. The data points are connected by B-splines for eye-guiding. The red curves are the mid-IR reflection-absorption spectra of corresponding SAMs taken from Ref. [43] for (a) and from Ref. [48] for (b). The insets show molecular structure of the samples. 54

Figure 4.9: Demonstration of spatial resolution. **(a)** Topography of the PEG monolayer islands acquired in contact mode. **(b)** Topographic line scan along the blue arrow in a, showing the height of the monolayer islands to be ~2 nm. **(c)** Mid-infrared photoexpansion spectra taken at the positions indicated in (b). The curves are labelled and colored in accordance with (b). Spectra are offset vertically for clarity. **(d)** Cantilever deflection signal at different points along the topographic scan in (b) for the laser tuned to the 1,342 cm^{-1} PEG absorption line (black) and to 1,552 cm^{-1}, away from the PEG absorption line (orange). Data points are extracted from spectra in (c). **(e)** Mid-IR mapping of monolayer islands: the lock-in output is recorded as a function of tip position for the mid-infrared laser wavelength fixed at the PEG CH_2 wagging absorption band at 1,342 cm^{-1}. Bright regions are PEG molecules and dark regions are gold. The image has 256 × 256 pixels and was obtained simultaneously with the topographic image in (a). The image was produced by raster scanning at a rate of 0.5 Hz with the lock-in integration time set to 3 ms. The total acquisition time was ~5min. **(f)** Signal along the line scan shown with a red arrow in (e). Data indicate a spatial resolution of ~25 nm for the image in (e)..57

Figure 4.10: Comparison of the background TSG spectrum (black) with the QCL power spectra taken by a MCT detector (red). 60

Figure 4.11: AFM topography scanning on PEG sub-monolayer islands sample before **(a)** and after **(b)** photoexpansion measurement carried out in Fig. 4.9...61

Figure 5.1: Two schemes of background suppression using two QCLs. **(a)** The suppression laser is operated in nearly cw mode **(b)** The suppression laser is operated in pulsed mode. The repetition frequency is same as that of the tunable laser, but two pulse trains have π phase delay. ...63

Figure 5.2: Schematic of the experimental setup for background-free photoexpansion nano-spectroscopy. QCL1 is the tunable laser and QCL2 is the suppression laser whose wavelength is fixed away from any sample absorption band. Two QCLs have the same pulse repetition frequency, by which the lock-in amplified is referenced. BS: beam splitter. 64

Figure 5.3: Cantilever signal recorded by lock-in as a function of the tunable laser power. The power was tuned via injecting different current. The power of the suppression laser was fixed. The dashed line is the calculated performance using Eq. (5.2) with $D = 0.5$.....................................66

Figure 5.4: Cantilever signal recorded by lock-in as a function of the phase delay between two laser pulses. The dashed line is the calculated performance using Eq. (5.2) with $a = b$..67

Figure 5.5: PEG monolayer spectrum acquired with (red) and without (black) the use of the suppression laser. The peak at 1342 cm^{-1} corresponds to the CH_2 wagging mode. 68

Figure 6.1: The dependence of tip-sample interaction force $F(z)$ (black curve) and heterodyne coefficient $F''(z)$ (red curve) on the tip-sample separation z. The curves are plotted using Eq. (2.1) with the parameters: effective intermolecular distance $a_0 = 0.24$ nm, Hamaker's constant $H = 14 \times 10^{-20}$ J, tip radius $R = 25$ nm, and reduced Young's modulus $E^* = 3$ GPa.72

Figure 6.2: Schematic of the experimental setup for photoexpasion nano-spectroscopy with heterodyne detection. The lock-in amplified is referenced at the difference frequency of laser pulse repetition and tip oscillation. FM: frequency mixer, BP: band pass filter. 73

Figure 6.3: Heterodyne signal generation and amplification. **(a)** Recorded cantilever responses in three cases: (top) only the laser was on, (middle) only the tip was oscillated, (bottom) both the laser and the tip oscillation were activated. The data was recorded with a spectrum analyzer. The QCL wavelength was tuned to PMMA's carbonyl peak at 1730 cm^{-1}. **(b,c)** Recorded heterodyne signal as a function of (b) the tip oscillation frequency and (c) the laser pulse repetition frequency. **(d)** Recorded heterodyne signal as a function of tip oscillation amplitude............75

Figure 6.4: Heterodyne photoexpansion spectra with 100 nm spatial resolution. **(a)** Top view of the testing sample. **(b)** AFM topographic image **(c,d)** Heterodyne photoexpansion spectra (red curves) of LOR (c) and PMMA (d) taken at the two locations marked in (b) with 100 nm separation. QCL pulse repetition frequency was ~600 kHz and the tip oscillated at ~800 kHz. The lock-in was referenced at ~200 kHz. **(e,f)** Conventional photoexpansion spectra (blue curves) of LOR (e) and PMMA (f) taken at the same locations with QCL pulses repeated at ~200 kHz and without tip oscillation...76

Figure 7.1: **(a)** AFM topography scanning of the chiral metasurface. **(b,c)** Surface current (arrows) and color-coded amplitude (left panel) of the normal electric field E_z from COMSOL simulations of normally incident RCP (b) and LCP (c) light waves...80

Figure 7.2: Schematic of experimental setup for mapping local optical energy distribution and ohmic heating on a chiral metasurface. The sample was illuminated by LCP/RCP light from a mid-IR QCL at normal incidence. QWP: quarter-wave plate..81

Figure 7.3: Photoexpansion microscopy measurements of circularly dichroic thermal expansion of the LOR-coated metasurface. **(a,b)** COMSOL simulations of the temperature increase distribution in the LOR film at the end of a square QCL pulse with time duration $T = 200$ ns and peak intensity $I = 1$kW cm^{-2} tuned to λ=9.1 μm, corresponding to the experimental conditions. **(c,d)** cantilever deflection on top of a LOR-coated sample excited with RCP (c) and LCP (d) laser pulses at normal incidence through the CaF_2 substrate. **(e)** Absorption spectrum of LOR polymer measured by FTIR. 82

Figure 7.4: Photoexpansion microscopy measurements of circularly dichroic thermal expansion of the polyethylene-coated metasurface. **(a,b)** COMSOL simulations of the temperature increase distribution in the polyethylene film at the end of a square QCL pulse with time duration $T = 200$ ns and peak intensity $I = 1$kW cm^{-2} tuned to λ=9.1 μm, corresponding to the experimental conditions. **(c,d)** cantilever deflection on top of a polyethylene-coated sample excited with RCP (c) and LCP (d) laser pulses at normal incidence through the CaF_2 substrate. **(e)** AFM topography scanning of the polyethylene-coated metasurface. 84

Figure 7.5: Photoexpansion microscopy measurements of circularly dichroic thermal expansion of the metasurface without polymer coating. **(a,b)** COMSOL simulations of the temperature increase distribution in the nanoantennas at the end of a square QCL pulse with time duration T = 200 ns and peak intensity I = 1kW cm^{-2} tuned to λ=9.1 µm, corresponding to the experimental conditions. **(c,d)** cantilever deflection on top of the metasurface excited with RCP (c) and LCP (d) laser pulses at normal incidence through the CaF$_2$ substrate............86

Chapter 1

Overview: Vibrational Nano-Spectroscopy

It is critical for many applications to identify and analyze chemicals at the nanoscale. Traditional far-field vibrational spectroscopy is a powerful analytical tool but only achieves diffraction-limited spatial resolution. The work presented in this dissertation focuses on developing a new nano-spectroscopy technique which is capable of characterizing infrared (IR) absorption of individual molecules non-invasively under ambient conditions.

1.1 MOLECULAR VIBRATION AND FINGERPRINT

Molecules are the building blocks of chemicals. They are composed of atoms and held together by chemical bounds. Due to its multiple degrees of freedom, a molecule can vibrate in many ways at different resonant frequencies, e.g. stretching, twisting and wagging, which are referred to as vibrational modes [1]. The molecular vibrational frequencies lie within the range of approximately 20–120 THz, corresponding to mid-IR wavelength λ = 2.5–15 μm (or expressed in wavenumber $\bar{\upsilon}$ = 667–4000 cm^{-1}). The specific values also depend on the mass of atoms and strength of bonds (single, double or triple). Therefore vibrational frequencies are unique parameters for each type of molecule and can be used as molecular fingerprint for chemical identification.

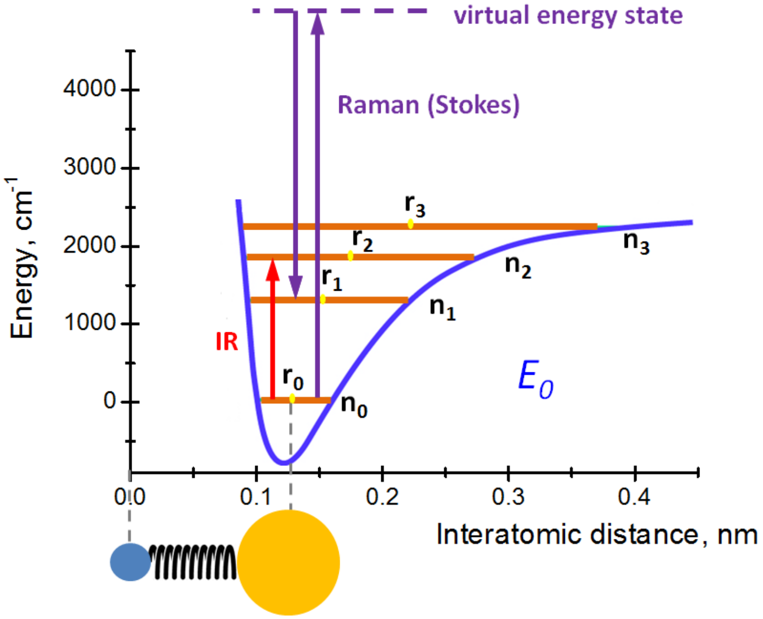
virtual energy state
Raman (Stokes)
4000
3000
2000
1000
0
Energy, cm^{-1}
IR
r_3
r_2
r_1
r_0
n_3
n_2
n_1
n_0
E_0
0.0
0.1
0.2
0.3
0.4
Interatomic distance, nm

Figure 1.1: Vibrational energy level diagram for an asymmetric diatomic molecule at the ground electronic state, with the transitions via IR absorption (red arrow) and Raman scattering (purple arrow) illustrated.

To further explain molecular vibration, we start from the simplest case, an asymmetric diatomic molecule. Its vibrational energy level diagram at the ground electronic state (E_0) is schematically shown in Fig. 1.1. The horizontal coordinate represents the separation between the two atoms, and the vertical coordinate is the energy level. The potential energy curve (blue) is formed as the consequence of interatomic attractive and repulsive interaction, with its second derivative being the effective spring constant of the chemical bond. Inside the potential curve, there exist multiple vibrational states (n_0, n_1, n_2 ...). The width of each state stands for the range in which the two atoms are allowed to separate during vibration (stretching in this particular case), and it increases with the mode number. The center of each state (r_0, r_1, r_2 ...) stands for the equilibrium position, in other words is the ‘volume’ of the molecule. A notable feature of this potential curve is it’s asymmetric, which results in the right-shift of the central position (molecular expansion) once the molecule is excited to a higher vibrational state. This simple fact is the starting point of the spectroscopy work presented in this dissertation. In the next section, we will discuss several optical techniques that can excite and detect molecular vibrations.

1.2 VIBRATIONAL SPECTROSCOPY

A vibrational mode can be excited optically when a molecule is polarized by the oscillating electric field of incoming light at its vibrational frequency. In this case the energy of a mid-IR photon is absorbed, and the molecule jumps to higher energy state from the ground state. This transition is illustrated by the red arrow in Fig. 1.1, with the possibility described by the IR absorption cross section σ_{IR}, which is typically on the order of 10^{-18}–10^{-21} cm^2 molecule^{-1} [2]. Another related parameter used at macroscopic scale is the absorption coefficient $\alpha = N\sigma_{IR}$, where N is the molecule number density in [molecule cm^{-3}]. The absorption coefficient α is also proportional to the imaginary part of refractive index κ by

$$\alpha = \frac{4\pi \cdot \kappa}{\lambda} \tag{1.1}$$

where λ is light wavelength. Equation (1.1) can be deduced from the definition of electromagnetic plane wave

$$E_0 e^{ikd} = E_0 e^{i\frac{2\pi}{\lambda}(n+i\kappa)d} = E_0 e^{-\frac{1}{2}\alpha d} \cdot e^{i\frac{2\pi}{\lambda}nd} \tag{1.2}$$

where E_0 is the amplitude of electric field, k is the wave vector, $n + i\kappa$ is the complex refractive index, and d is the wave propagation distance. From Eq. (1.2), we know that α represents the attenuation constant for light intensity and its value can be determined experimentally according to the Beer–Lambert law

$$I_d = I_0 e^{-\alpha d} \tag{1.3}$$

where I_d and I_0 are the transmitted and incident light intensity, respectively.

A plot of the absorption coefficient as a function of light wavelength $\alpha(\lambda)$ represents an IR absorption spectrum, on which one could see many peaks (or dips) corresponding to the excited vibrational modes of a molecule. For solids samples in which molecules have complicated structure and strongly interact with each other, closely neighboring absorption peaks are broadened to form wide absorption bands, while for simple gas molecules there are sharp and isolated absorption lines shown on the spectrum.

For practical IR spectra acquisition, Fourier transform infrared (FTIR) spectroscopy [3] has been the most widely used technique. Absorption spectra of numerous chemicals have been collected to establish extensive reference databases. FTIR is based on the interference detection over wide spectral range simultaneously. The light source is a Globar usually made of SiC. When electrically heated up to over ~1300 K, it emits similar to black-body radiation which covers all the IR wavelengths with moderate intensity. This broadband beam then splits into two paths. On one path, light is partially absorbed by the sample through transmission or reflection, while on the other path (reference path), light is reflected by a fast moving mirror. In the end, the two beams interfere at the photodetector position. At each mirror position, constructive interference only occurs for some wavelengths. By recording the photodetector signal as a function of mirror positons, which are then Fourier transformed to the wavelength domain, an IR absorption spectrum is obtained. On the FTIR spectrum, the vertical coordinate stands for the absorbance that is defined by

$$A = -\log_{10}\frac{I_d}{I_0} \approx 0.43 \cdot \alpha \cdot d \qquad (1.4)$$

Compared to the monolithic spectrometer, FTIR has the advantages of fast spectra acquisition and better signal-to-noise ratio improved by a factor of $\sqrt{N}$, where N is the number of repeated measurements [3].

Vibrational transitions via IR absorption must obey selection rules [2], which prohibits IR spectroscopy from probing all the vibrational modes. For instance, nonpolar molecules do not have IR active modes [2]. A complimentary optical method to excite molecular vibration with different selection rules is Raman scattering. This process occurs when high-energy photons (from near-IR to ultraviolet) are inelastically scattered by the molecules. First, oscillating electric field of incident light polarizes a molecule at very high frequency to a virtual energy level (see the purple arrow in Fig. 1.1). Then it is possible for this molecule polarization to couple with the vibrational states different from the initial state. If that happens, photons will be re-emitted but with the energy differs by the exact amount needed to excite that vibration mode. Since most molecules occupy the ground vibrational state by Boltzmann distribution, usually the scattered photons have lower energy (Stokes scattering). Raman scattering is a very inefficient process with the typical Raman cross section σ_{Raman} being only ~10^{-30} cm^2 $molecule^{-1}$ [2]. One advantage of Raman spectroscopy is it uses one monolithic laser source to excite all the allowable vibrational modes of molecules. To form a Raman spectrum, the scattered photons which have different wavelengths are dispersed to a photodetector array (CCD or CMOS) by a diffraction gating, so that each detector element records light intensity at the perspective wavelength simultaneously.

1.3 CURRENT NANO-SPECTROSCOPY TECHNIQUES

In conventional spectroscopy, light is focused onto a sample in free space by lens or focusing reflector. Due to the far-field diffraction limit [3], the dimension of the focused spot, which determines lateral resolution for spectral measurement, cannot be smaller than approximately $\lambda/2n$, where n is the refractive index. This prohibits powerful chemical analysis of FTIR and Raman from being applied on nanoscale research objects, for example investigating how drug molecules target and react inside a diseased cell. Other important nano-samples in material and life sciences include but not limited to carbon nanotube (5–50 nm in diameter), copolymer (<50 nm in domain spacing), protein (<50 nm in diameter), virus (20–400 nm in diameter) and DNA strands (only 2.5 nm in diameter). Vibrational spectroscopy technique with nanometer spatial resolution (*nano-spectroscopy*) therefore is highly desired. In this section, we briefly discuss current nano-spectroscopy techniques which include tip-enhanced Raman Spectroscopy (TERS), scattering-type near-field scanning optical microscopy (s-NSOM), and IR photoexpansion nano-spectroscopy (also termed as AFM-IR). All of the three techniques operate by using a sharp scanning probe whose dimension is only 5–30 nm in radius (usually an atomic force microscopy (AFM) tip). The spectral signal comes from local tip-sample interaction, and by raster scanning the sample at selected wavelengths, chemical images can be generated.

Currently, TERS [4–8] is the only vibrational spectroscopy technique that has been demonstrated with single-molecule sensitivity, despite the fact that σ_{Raman} is by many orders of magnitude lower than σ_{IR}. Such extreme sensitivity benefits from the unique signal enhancement mechanisms that are not available with mid-IR absorption measurement. First, local plasmon resonance is excited in the metallized AFM tip in the visible range. The tip, in the first-order approximation, can be treated as a metal sphere with complex permittivity ε_M surrounded by the dielectric medium with $\varepsilon_D \sim 1$. The metal sphere's polarizability will reach a maximum value when $Re(\varepsilon_M) = -2\varepsilon_D$ (Clausius–Mossotti relation) [9,10], which can only be satisfied in the visible range contributed from the interband transition of electrons. Second, the tip enhancement works twice for both the incident and the Raman scattered photons. As a result, the Raman signal is proportional to the fourth power of the enhancement of local electric field $|E/E_0|^4$. In contrast, the dependence is only $|E/E_0|^2$ for mid-IR absorption.

S-NSOM [11–14] is the most common technique for mid-IR spectroscopy and microscopy at the nanoscale. This technique can produce chemical images in mid-IR with spatial resolution of ~λ/300 or better from samples as thin as a monolayer. In s-NSOM, incident light induces a strong electric dipole in a metalized AFM tip, which in turn induces an image dipole in the local sample, whose polarizability is a function of its complex permittivity ε_s. The local ε_s is then encoded in the far-field radiation of the coupled tip-sample dipoles (referred to as the tip signal) and measured by a photodetector. Because the tip signal has highly nonlinear dependence on the tip-sample separation, despite being very small, it can be distinguished from the strong background light scattered by the tip shaft and the nonlocal sample, via tapping the tip at frequency ω but demodulating the photodetector signal with sophisticated homodyne- or heterodyne-based optical setups. From the collected s-NSOM amplitude and phase signal, the imaginary part is computed, which approximates the imaginary part of refractive index κ under the low resonance approximation [12,15].

IR photoexpansion nano-spectroscopy, which is presented in this dissertation, is the third technique. Its principle is based on the simple facts that a sample will experience quick thermal expansion upon IR pulse excitation, and the induced expansion force acting on an AFM tip will lead to the cantilever deflection with an amplitude proportional to sample's absorption. By reading cantilever deflection from the built-in position detector of AFM when scanning laser wavelength, one obtains a photoexpansion spectrum which is equivalent to a mid-IR absorption spectrum. The challenge of this new opto-mechanic approach is to make thin sample expansion detectable while not causing photothermal damage. The first demonstration carried out in 2005 by Dazzi. *et al.* [16] used high power laser pulses yet could only be applied to relatively thick samples (on the order of 100 nm). With some tricks we have developed in this dissertation [17,18], now this technique is capable of acquiring monolayer expansion signal from a sample area of sub 100 nm^2. Photoexpansion nano-spectroscopy also features simple setup without using an external mid-IR photodetector (which works at the cryogenic temperature).

1.4 DISSERTATION OVERVIEW

The dissertation is organized as follows.

In Chapter 2, we introduce some basic mechanics of AFM cantilever which is related to photoexpansion measurement. We first discuss the origin of sample photoexpasion force. Upon force action, the cantilever starts to oscillate. We then explain how the cantilever oscillation is monitored and calibrated in an AFM system. After that, different cantilever resonant modes are examined, in particular those excited when the tip is in contact with sample surface. To know the detection limit of AFM, cantilever thermal noise is briefly discussed in the last section.

Chapter 3 reports the first experiment to improve photoexpansion sensitivity by matching IR pulses from a quantum cascade laser (QCL) with the cantilever resonance. Photoexpansion spectra are acquired with low sample heating. A harmonic oscillator model is used to estimate cantilever deflection amplitude when in resonance.

Chapter 4 reports the first experiment to demonstrate monolayer sensitivity by employing both cantilever resonance enhancement and tip enhancement. Detailed analysis of tip enhancement in mid-IR region is provided.

In Chapter 5, we propose to use a second QCL to suppress high background signal presented in the monolayer spectra acquired in Chapter 4. This method could help to demonstrate higher detection sensitivity in the future.

In Chapter 6, we explore the nonlinear interaction between sample photoexpansion and cantilever's self-oscillation, and are able to generate sample photoexpansion signal at the heterodyne frequency.

Chapter 7 demonstrates that photoexpansion microscopy can be used for mapping local light intensity distribution and ohmic heating of plasmonic metasurface.

Chapter 8 concludes the work presented in this dissertation and briefly discusses the future of this technique.

Chapter 2

AFM Basics for Photoexpanison Measurement

2.1 INTRODUCTION

Upon mid-IR photon absorption, molecules transit into an excited vibrational state. In a very short time (~ 10 ps [19]), the excited vibrational mode non-radiatively dissipates into other vibrational modes of lower energies as well as to vibrational and kinetic modes of the surrounding molecules and the substrate. Because of the anharmonicity of molecular vibrations as illustrated in section 1.1, the effective molecular volume increases. On a macroscopic scale this leads to sample's thermal expansion.

At the time of photoexpansion, if an AFM tip is in contact with the sample, an expansion force will be exerted on the tip and results in cantilever deflection. Though AFM is a sensitive instrument, it is still difficult to measure the cantilever deflection caused by thin film (<1 μm) photoexpansion. The linear thermal expansion coefficient for typical polymers is on the order of 10^{-4} K^{-1} [20]. This means for a 100 nm-thick film if heated by 10 K, the expansion is only 1 Å. In principle, in order to have a detectable photoexpansion signal, the expansion force needs to do a work to the cantilever at least greater than the thermal noise energy k_BT. Much effort of this dissertation has been put to generate adequately large photoexpasion force from ultra-thin samples for the given laser power, and efficiently translate the sample photoexpansion to AFM cantilever deflection. Before we discuss those results, it is necessary to introduce some basic cantilever mechanics related to the photoexpansion measurement. The topics include the

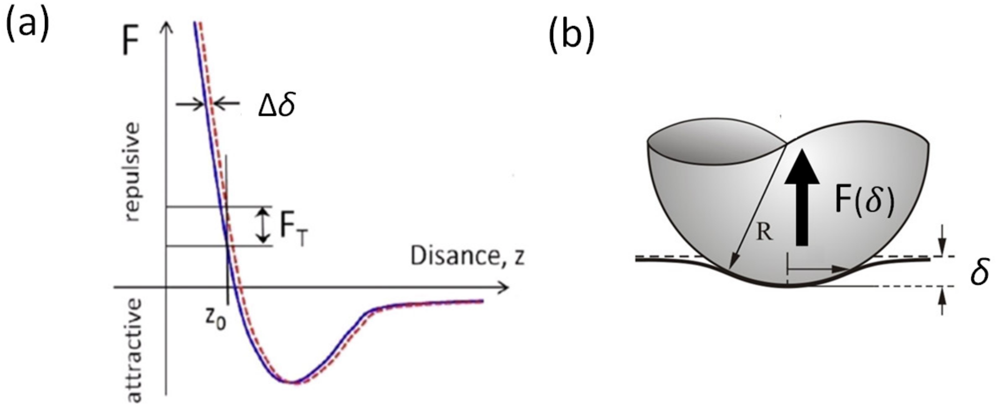

Figure 2.1: **(a)** Mechanism of AFM cantilever deflection during sample photoexpansion. Blue solid curve shows the dependence of the interaction force between the sample surface and the AFM cantilever tip on tip-surface distance (z). Red dashed curve is shifted along z-axis by sample photoexpansion $\Delta\delta$. F_T is the photoexpansion force acting on the AFM cantilever; z_0 is the position of the AFM cantilever in contact mode. The figure is not drawn to scale. **(b)** Illustration of contact between a tip and an elastic sample plane. The repulsive tip-sample force is generated by the sample indentation δ.

origin of photoexpanison force, cantilever resonances, the effect of sample coupling on the cantilever behavior and lastly cantilever's thermal noise.

2.2 ORIGIN OF PHOTOEXPANSION FORCE

The origin of photoexpansion force can be explained intuitively in Fig. 2.1(a). The blue curve represents the dependence of tip-sample interaction force F on their separation z, with z_0 being the equilibrium position of the AFM tip in contact mode. Upon IR pulse excitation, sample photoexpansion happens on a time scale much shorter than the mechanical response time of the AFM cantilever (~5 µs). This means the tip's position does not change immediately after photoexpansion. Thus the force curve is shifted along z-axis to the red one by the amount of sample expansion $\Delta\delta$. As a result, the tip feels a larger repulsive force at z_0 and the difference F_T is the photoexpansion force.

Next, we quantify the photoexpansion force. Here we consider the tip as a rigid sphere with radius R, and the sample as an elastic plane (see Fig. 2.1 (b)). According to the Derjaguin-Muller-Toporov (DMT) model [21,22], the AFM tip has adhesive elastic contact with the sample surface. That is to say when in contact, the middle part of the tip feels repulsive force due to sample's elastic deformation, while the outside wall of the tip (which is not in direct contact) is attracted to the sample by van der Waals force. The total tip-sample interaction force is given by

$$F(z) = \frac{4}{3}E^{*}R^{1/2}(a_0 - z)^{3/2} - \frac{HR}{6a_0^2} \qquad (z \le a_0) \qquad (2.1)$$

where a_0 is introduced as the effective intermolecular distance. It means at $z = a_0$, the tip just jumps out of the contact with sample surface, hence $F(a_0) = -HR/6a_0^2$ represents the pull-off force from sample adhesion. $\delta = a_0 - z$ stands for the indentation. E^* and H are the reduced Young's modulus and Hamaker's constant, respectively. These two parameters are determined by material. As we can see from Eq. (2.1), the interaction force has nonlinear dependence on the indentation δ. Assuming sample expansion $\Delta\delta$ is much smaller than δ, the photoexpansion force F_T can be derived from Eq. (2.1) in the first-order approximation to be

$$F_T \approx 2E^{*}R^{1/2}\delta^{1/2}\Delta\delta \qquad (2.2)$$

By plugging typical parameters into Eq. (2.2), we find F_T is on the order of 100 pN.

2.3 DETECTION AND CALIBRATION OF CANTILEVER DEFLECTION

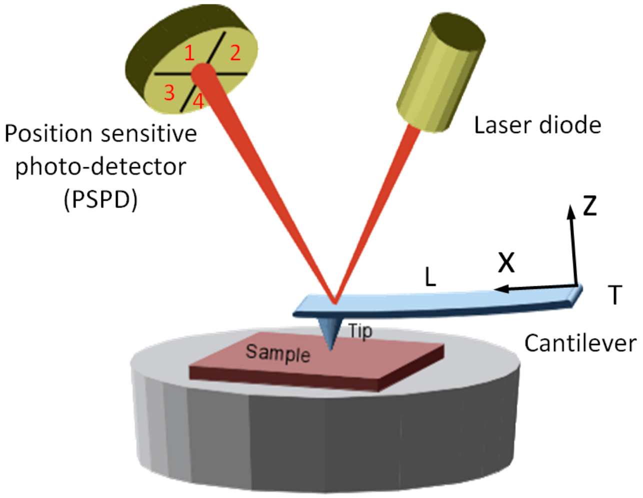

Figure 2.2: Schematic of AFM configuration. The cantilever deflection is measured by an optical level system which is composed of a visible laser beam and a position sensitive photodetector (PSPD).

The photoexpansion force pushes an AFM cantilever up to produce an initial cantilever deflection. The cantilever then undergoes linear oscillation around its equilibrium position. In AFM, cantilever motion is measured by the optical level system in which a visible laser beam is reflected from the backside of the cantilever to a position-sensitive photodetector (PSPD) (see Fig. 2.2). The change of beam reflection angle thus is proportional to the cantilever deflection.

PSPD is composed of four independent photodiodes (marked by '1–4') with each responding differently to its overlap with the laser beam spot. By doing some math, the PSPD Voltage V_{PSPD} can quantify either flexural ($V_1 + V_2 - (V_3 + V_4)$, 'A-B' signal) or torsional ($V_1 + V_3 - (V_2 + V_4)$, 'C-D' signal) deflection of the cantilever. When performing photoexpansion spectroscopy/microscopy with IR pulses, the AC component of V_{PSPD} represents sample absorption signal while the DC component is used as the contact-mode feedback to scan sample topography.

It is worth noting that what the optical level directly measures is not the cantilever deflection amplitude but the cantilever inclination (namely "optical sensitivity" [23]). Under the static condition, i.e. when the cantilever is deflected by a constant force, these two quantities are linearly related by [24]

$$dz(L) = \frac{2L}{3}\frac{dz(L)}{dx} \tag{2.3}$$

where L is the cantilever length, so $dz(L)$ stands for cantilever deflection amplitude at the tip end and $dz(L)/dx$ stands for cantilever inclination, according to the coordinate system shown in Fig. 2.2.

Practically, the calibration between PSPD voltage V_{PSPD} and cantilever deflection amplitude $dz(L)$ can be obtained by performing a force-distance curve measurement on hard sample surface, e.g. Si wafer. During the force curve acquisition, the cantilever is brought into contact with sample by the piezoelectric transducer, with V_{PSPD} being recorded as a function of the piezo position. The dependence will be linear in the contact region because the hard sample surface does not deform. On the other hand, the piezo positon change during contact is considered to be the same as $dz(L)$, so a calibration coefficient in [nm V^{-1}] between V_{PSPD} and $dz(L)$ is established. This number, however, is only valid for the first bending mode of the cantilever in free space. To deduce the deflection amplitude in a photoexpasion experiment, in which the cantilever is in contact with sample and usually operated at the second or higher-order bending mode, we need to discuss the cantilever resonances first.

2.4 CANTILEVER BENDING MODES

2.4.1 In free space

Here we only discuss rectangular-shaped cantilevers. A typical contact-mode AFM cantilever used in our experiments has the dimension of $L \times w \times t = 450 \times 50 \times 2$ μm and a spring constant of 0.2 N m^{-1} (ContGB-G, Budget Sensors). Neglecting the tip mass, the AFM cantilever is treated as a homogeneous rectangular beam with one end fixed and the other end (tip end) free-standing or coupled to sample surface. As long as $t \ll w$, the cantilever's flexural deflection is described by the Euler–Bernoulli equation [25] using the coordinate system illustrated in Fig. 2.2

$$EI\frac{\partial^4 z}{\partial x^4}+\rho A\frac{\partial^2 z}{\partial t^2}=0 \tag{2.4}$$

where E is the Young's modulus of cantilever material (usually made of Si or Si_3N_4), ρ is the mass density, $A = wt$ stands for the cross-section area, and $I = wt^3 / 12$ is the area moment of inertia. To solve Eq. (2.4), one could assume a general solution with the harmonic time dependence as $z(x,t) = z(x)e^{-i\omega t}$, so that the spatial and time variables are separated. The analytical spatial solution of Eq. (2.4) is quoted [25] as

$$\begin{aligned} z_n(x) = z_n^0((&\cos\beta_n x - \cosh\beta_n x) \\ &-\frac{\cos\beta_n L + \cosh\beta_n L}{\sin\beta_n L + \sinh\beta_n L}(\sin\beta_n x - \sinh\beta_n x)) \end{aligned} \tag{2.5}$$

where z_n^0 and β_n are the vibrational amplitude and the wave number at the nth bending mode, respectively. In the case of free-standing tip end, the corresponding boundary conditions are

$$\begin{cases} z(0) = 0 & \text{(no motion at } x = 0\text{)} \\ \dfrac{\partial z(0)}{\partial x} = 0 & \text{(no slope at } x = 0\text{)} \\ \dfrac{\partial^2 z(L)}{\partial x^2} = 0 & \text{(no moment at } x = L\text{)} \\ \dfrac{\partial^3 z(L)}{\partial x^3} = 0 & \text{(no shear force at } x = L\text{)} \end{cases} \tag{2.6}$$

which yields the characteristic equation of β_n to be

$$\cos \beta_n L \cosh \beta_n L + 1 = 0 \tag{2.7}$$

The solutions for Eq. (2.7) are obtained numerically. $\beta_1 L = 1.875$, $\beta_2 L = 4.694$ and $\beta_3 L = 7.855$ for the first three bending modes. With these, the resonant frequencies are readily given by

$$f_n = \frac{(\beta_n L)^2}{2\pi L^2 (\rho A / EI)^{1/2}} \tag{2.8}$$

The cantilever shapes for the first three bending modes in free space are plotted in Fig. 2.3(a) by using Eqs. (2.5) and (2.7). The respective resonant frequencies are calculated using Eq. (2.8). It is noted that the optical sensitivity (slope at the tip end) increases with the mode number. But in the experiment, V_{PSPD} may also be affected by the reflected laser beam position on the cantilever. The beam spot size is about 30 μm in diameter in our AFM system. When operating at higher-order mode, one should avoid aligning the beam to the minimum slope region.

To excite cantilever bending modes, it is required that the input energy has Fourier components at those resonant frequencies. There are three types of excitation in the photoexpansion measurement. First, the $k_B T$ energy a cantilever acquires from room

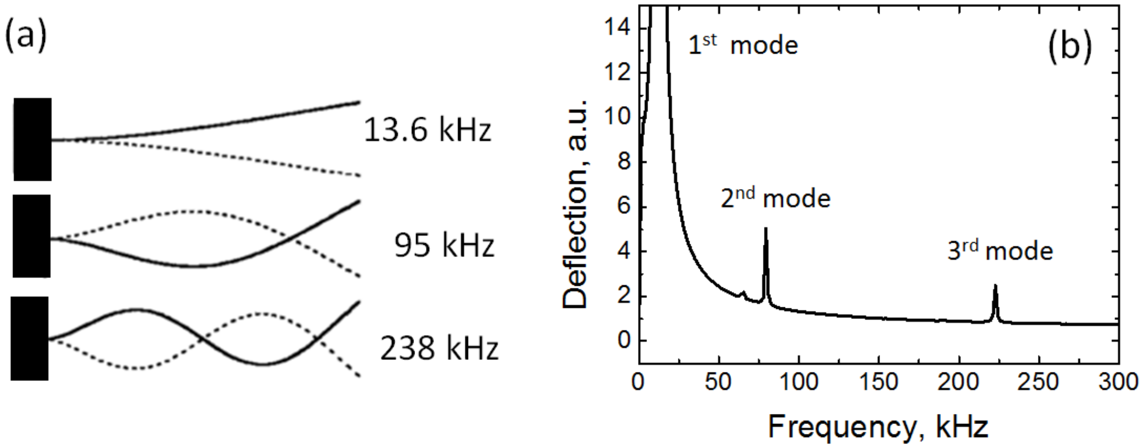

Figure 2.3: Cantilever resonances in free space. **(a)** Cantilever shape for the first three bending modes calculated using Eqs. (2.5) and (2.7). The corresponding eigenfrequencies are calculated using Eq. (2.8) for a ContGB-G cantilever. **(b)** Measured noise spectrum of that cantilever.

temperature will excite all the resonant modes, which contributes to the thermal noise. Figure 2.3 (b) shows the noise spectrum of a ContGB-G cantilever measured in free space, with the resonance frequencies close to the calculated value in Fig. 2.3(a). Second, pulsed expansion force that is repeated much slower than the cantilever resonances will also excite all the modes. This case corresponds to when a mid-IR source with low pulse repetition frequency is used. Since the vibrational energy of the cantilever due to the force action is distributed to all the modes, it is not efficient. And third, particular cantilever mode is excited by expansion force directly repeated at that mode’s frequency. This case corresponds to when a mid-IR source with high and adjustable pulse repetition frequency is used.

Another two important cantilever parameters related to photoexpansion measurement are the effective spring constant k_n and the cantilever quality factor (Q-factor). The static spring constant is calculated by $k_1 = Ew^3t/4L^3$ [25]. At higher order modes, the effective spring constant becomes $k_n = (f_n/f_1)^2 \cdot k_1$, where f_n is given in Eq. (2.8). So the cantilever becomes stiffer at higher modes, which means smaller cantilever deflection amplitude upon the same force action. Q-factor characterizes the ability of a cantilever to build up resonant deflection amplitude, and is determined by the energy loss due to various mechanisms, including air damping and support loss when in contact with the sample, so $1/Q = 1/Q_{damp} + 1/Q_{support} + 1/Q_{other}$ [26].

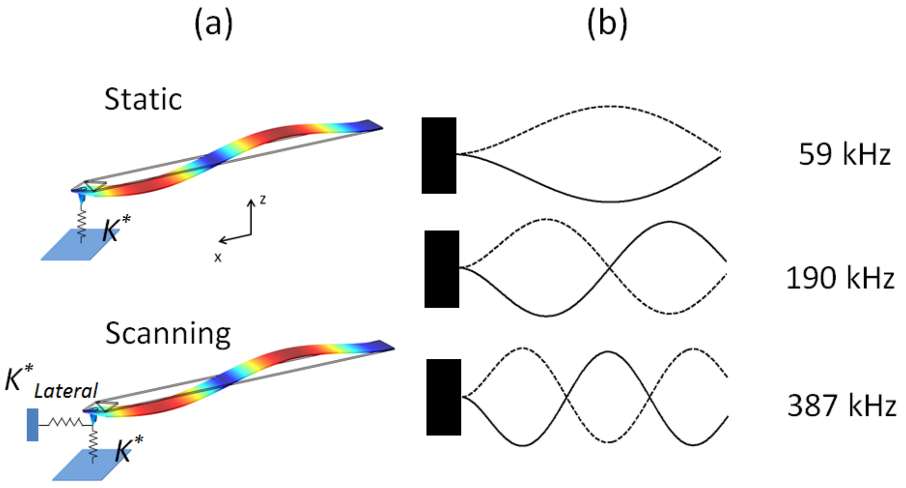

Figure 2.4: Cantilever resonances when in contact with the sample. **(a)** The vertical and lateral tip-sample interactions are approximated with the effective spring constants $k*$ and $k*_{Lateral}$. **(b)** Cantilever shape for the first three bending modes when k^{*}/k_{1}=1,000, calculated using Eqs. (2.5) and (2.10).

2.4.2 In contact with sample

To measure sample photoexpansion, the AFM tip needs to be in contact with the sample. The tip-sample interaction force $F(z)$ (Eq. (2.1)) results in an effective spring $k^{*} = -dF(z)/dz$ attached to the cantilever with its physical picture presented in Fig. 2.4(a). In this case, the boundary conditions changes to [25]

$$\begin{cases} z(0)=0 & \text{(no motion at } x=0\text{)} \\ \dfrac{\partial z(0)}{\partial x}=0 & \text{(no slope at } x=0\text{)} \\ \dfrac{\partial^{2} z(L)}{\partial x^{2}}=0 & \text{(no moment at } x=L\text{)} \\ \dfrac{\partial^{3} z(L)}{\partial x^{3}}=\dfrac{k^{*}}{EI}\text{z(L)} & \text{(with shear force at } x=L\text{)} \end{cases} \tag{2.9}$$

Accordingly, the characteristic equation for the wavenumber β_n becomes

$$\begin{aligned}&\sinh\beta_n L\cos\beta_n L-\sin\beta_n L\cosh\beta_n L\\&=\frac{(\beta_n L)^3 k_1}{3k^*}(1+\cos\beta_n L\cosh\beta_n L)\end{aligned}\tag{2.10}$$

The $\beta_n L$ values solved by Eq. (2.11) are larger than those of the free space case given by Eq. (2.6), and increase with k^*. For example, when $k^*/k_1 = 1{,}000$, we have $\beta_1 L = 3.917$, $\beta_2 L = 7.007$ and $\beta_3 L = 10.012$. This leads to two consequences:

(a) Cantilever shape is changed. Using Eq. (2.6) with new $\beta_n L$, the first three bending modes are plotted schematically in Fig. 2.4(b). As we can see, due to the tip-sample interaction, the tip end of the cantilever is effectively clamped.

(b) Cantilever resonances shift to higher frequencies according to Eq. (2.7). These are referred to as contact resonances. The frequency of n-th order contact resonance is between the n-th and (n+1)-th order free resonances [25]. Using the expression of tip-sample interaction force in Eq. (2.1), the effective spring constant can be expressed as $k^* = 2E^* R^{1/2}\delta^{1/2}$. One may expect that the contact resonant frequency will increase with the indentation δ (caused by stronger AFM setpoint force). In the experiments, k^* is also affected by the adhesion force. That happens when the tip oscillates away from the sample surface. Figure 2.5 shows a force-distance curve measured on PMMA polymer film, in which the adhesion force reads to be 30 *nN*, while the setpoint force used is 10 *nN*. For an inhomogeneous sample, adhesion can vary point by point due to different chemical composition or morphology, so is the contact resonance frequency. In addition, when the tip is raster scanning sample surface in the contact mode, the lateral force interaction is approximated with another effective spring constant $k^*{}_{Lateral}$ (see Fig. 2.4(a)), which will also shift cantilever resonance frequencies.

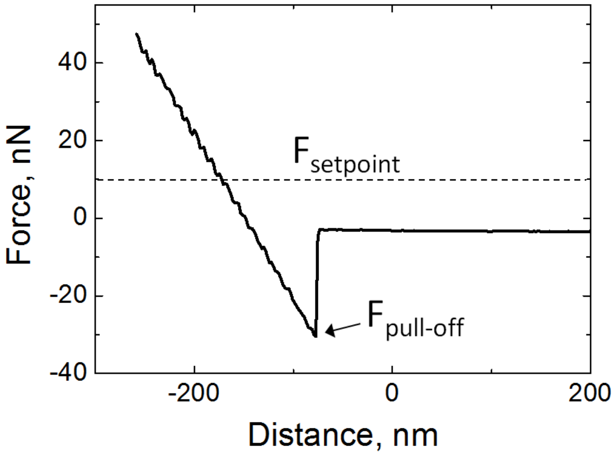

Figure 2.5: AFM Force-distance curve measured on a 300 nm-thick PMMA film. Sample adhesion force $F_{pull\text{-}off}$ and contact mode setpoint force $F_{setpoint}$ are compared.

2.4.3 Deduce cantilever deflection amplitude in contact resonance

In our photoexpansion measurement, the cantilever typically operates at the second bending mode. To determine the deflection amplitude, we need to compare the slope of the tip end for the first free bending mode with the slope of the tip end for the second bending mode in contact with the sample. The procedure is described as follows.

For the first free bending mode of the cantilever, the cantilever shape is given by Eq. (2.6) with $\beta_1 L = 1.875$. For the second bending mode in contact with the sample we need to take into account the force constant of the tip-sample interaction k^*. Its value could be experimentally deduced by the resonant frequency shift from free space to sample contact. For a ContGB-G cantilever, we observe the frequency of the second bending modes shifts from ~90 kHz to ~200 kHz, which results in $k^* = 200$ N m^{-1} and $\beta_2 L \approx 7$ according to Ref. [25]. Since the PSPD voltage is only determined by the slope of the cantilever, we obtain

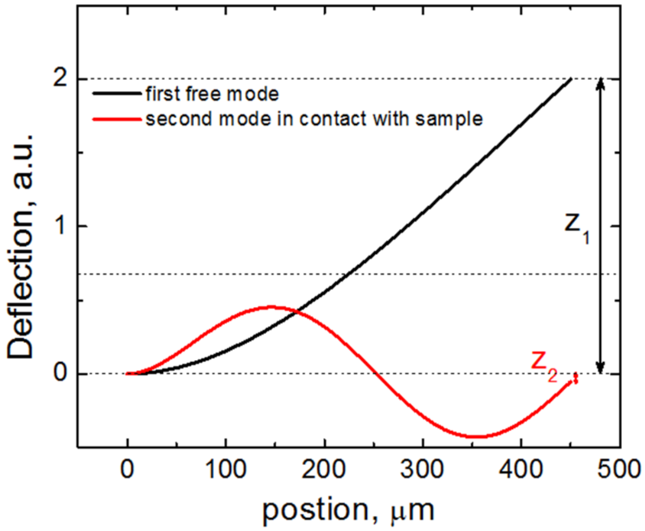

Figure 2.6: Comparing the cantilever deflection amplitude between the first bending mode in free space (black) and second bending mode in contact with the sample (red), with the same PSPD output voltage (slope of the tip end).

$$\begin{aligned} V_{PSPD} &= K \left.\frac{dz_1}{dx}\right|_{x=L} \times z_1 \\ V_{PSPD} &= K \left.\frac{dz_2}{dx}\right|_{x=L} \times z_2 \end{aligned} \qquad (2.11)$$

where K is the proportionality constant between PSPD voltage and the slope of the tip end $\left.\frac{dz_i}{dx}\right|_{x=L} \times z_i$. The derivatives can be calculated from Eq. (2.5). Comparing the derivatives in Eq. (2.11), we then obtain that z_1 cantilever deflection in the first bending mode produces the same PSPD signal as the second bending mode with $z_2 \approx z_1/35$ deflection. This is also illustrated in Fig. 2.6 where the two modes have the same slope and the respective deflection amplitude z_1 and z_2 are compared. Finally, with the known optical sensitivity obtained in section 2.3, we are able to convert PSPD voltage to the deflection amplitude z_2 in nm.

2.5 CANTILEVER THERMAL NOISE

In thermal equilibrium, each cantilever mode has a mean thermal energy of $1/2k_BT$ = 13 meV [27], which makes the cantilever oscillate at a small amplitude. This limits the lowest signal level one could detect from AFM. The thermal noise amplitude at the n-th order bending mode is quoted [27] as

$$z_n = \sqrt{\frac{12k_BT}{k_1(\beta_nL)^4}} \tag{2.12}$$

Two conclusions could be made from Eq. (2.12):

(1) Thermal noise is smaller for stiffer cantilevers as $z_n \propto (k_1)^{-1/2}$. k_1 is mainly determined by the ratio of cantilever width to the length as discussed previously.

(2) Thermal noise drops quickly when the cantilever is in contact with sample or at higher order resonance. In both cases, the value of β_nL increases and $z_n \propto (\beta_nL)^{-2}$. For a ContGB-G cantilever, k_1 = 0.2 N m^{-1}, $\beta_2L \approx 7$ (second contact resonance), hence we have $z_2 \approx$ 10 pm.

Chapter 3

Cantilever Resonance Enhanced IR Nano-Spectroscopy with QCL

3.1 INTRODUCTION

A sharp AFM tip alone does not necessarily guarantee nanometer spatial resolution for IR photoexpansion measurement. In 2000, Anderson [28] first proposed to use an AFM cantilever in contact mode as a light absorption detector. In his demonstration, the cantilever deflection followed the slowly-changed sample surface deformation induced by a FTIR broadband source chopped at 3 Hz. Nanoscale chemical characterization, however, is not likely to be achieved on his setup, because the long-time radiation (0.15 sec) will result in a considerably long thermal diffusion length which kills the spatial resolution. In that case, the cantilever could be deflected due to the heat diffused from the non-local sample.

The key to achieve nanoscale resolution with an AFM tip is to heat the sample with short IR pulses, usually from a laser. Thermal diffusion length L_d is determined by sample's heat diffusivity and the light pulse width as

$$L_d = \sqrt{\frac{k}{\rho C} \cdot \tau} \tag{3.1}$$

where k, ρ, and C are the thermal conductance, mass density and heat capacity of the sample, respectively, and τ is the duration of light pulse. For typical polymers $k = 0.5$

Portions of this chapter have been published in Lu, F. & Belkin, M.A. Infrared absorption nano-spectroscopy using sample photoexpansion induced by tunable quantum cascade lasers, *Opt. Express* **19**, 19942 (2011).

W m^{-1} K^{-1} and $\rho C = 2$ J cm^{-3} K^{-1} [20], we then have $L_d < 100$ nm for sub-100 ns pulses. In this regard, conventional mid-IR laser sources like CO_2 laser and optical parametric oscillator (OPO) which can output 10 ns-long pulses are good candidates. They have been successfully employed to perform nanoscale IR photoexpansion spectroscopy [16,29,30] and the broadly tunable OPO has been integrated into a commercial AFM-IR system (nanoIR^{TM}, Anasys Instruments). However, the disadvantage of using these lasers is they have very low pulse repetition frequency compared to the AFM cantilever resonances, so the detection sensitivity is limited.

In this chapter, we focus on improving the photoexpansion sensitivity with cantilever resonance enhancement. This is achieved when the sample is illuminated by IR pulses from a quantum cascade laser (QCL) repeated precisely at the cantilever resonant frequency. We can acquire high-quality absorption spectra with much lower sample heating than that induced by a CO_2 laser or OPO.

3.2 PROTOTYPE OF PHOTOEXPANSION NANO-SPECTROSCOPY

The first demonstration of nanoscale photoexpansion spectroscopy was carried out by Dazzi, *et al.* [16] in 2005 using a CO_2 laser and a free electron laser (FEL). The commercialized setup based on their approach is shown in Fig. 3.1(a). Thin film samples are prepared on top of a ZnSe prism (IR transparent, refractive index $n \approx 2.4$), and illuminated by a broadly tunable OPO in its evanescent field. The OPO outputs pulses at 1 kHz repetition frequency. Each pulse excitation gives the AFM cantilever initial momentum to oscillate around its equilibrium position (see Fig. 3.1(b)). Due to air damping, the cantilever undergoes ring-down oscillation. The recorded deflection signal

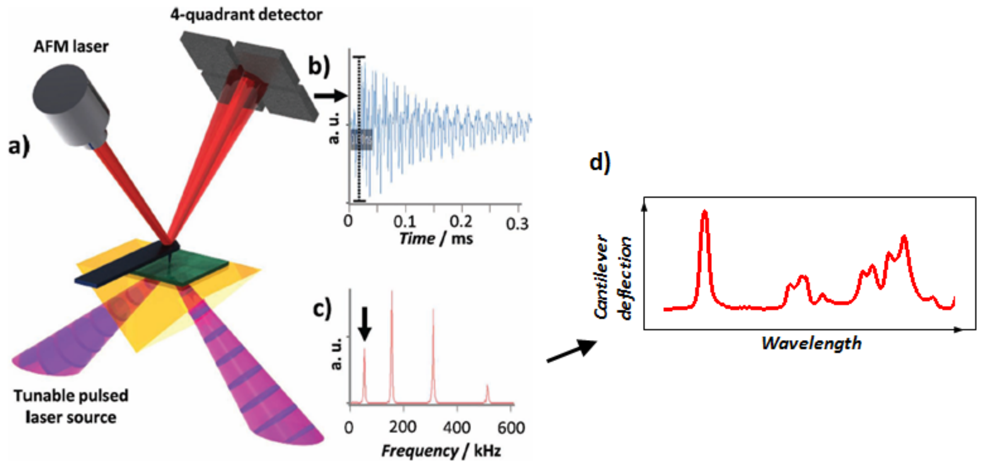
4-quadrant detector
AFM laser
a)
b)
a. u.
0
0.1
0.2
0.3
Time / ms
c)
a. u.
0
200
400
600
Frequency / kHz
Tunable pulsed
laser source
d)
Cantilever deflection
Wavelength

Figure 3.1: Setup and signal extraction in prototype photoexpansion nano-spectroscopy. **(a)** Schematic setup. **(b)** Recorded cantilever ring-down oscillation induced by one mid-IR pulse. **(c)** Corresponding frequency domain signal by applying Fourier transform on (b). **(d)** Absorption spectrum obtained via tuning the laser wavelength. This set of figures was acquired from Anasys Instruments.

is then Fourier transformed to the frequency domain in Fig. 3.1 (c) where we can see that all the cantilever bending modes are excited and they are on the order of 100 kHz. To generate an IR absorption spectrum, a band pass filter is usually applied to one bending mode and the mode amplitude is recorded as a function of the OPO wavelength (Fig. 3.1(d)).

This approach has relatively low detection sensitivity because of two aspects. First, as we can see from Fig. 3.1(b), the amplitude of cantilever ring-down oscillation drops quickly to the noise level in about 0.3 ms, but the period between two IR pulses is as long as 1 ms. This results in a low and noisy time-averaged cantilever signal. Second, the cantilever vibrational energy induced by laser pulses is distributed to all the cantilever modes, but only one mode is used to contribute to the sample signal.

Effort has been made for improving this prototype approach. Felts, *et al.* [31] reported that the cantilever vibrational energy is more likely to be distributed to the lower-order resonances for large-volume samples and distributed to higher-order resonances for small-volume samples, so averaging the cantilever deflection signal in a proper time and frequency window can help to improve the signal-to-noise ratio.

Nevertheless, due to the inherent disadvantage of using slowly repeated IR pulses, only relatively thick samples (~15 nm thick or thicker [31]) produced detectable cantilever deflections, even when the mid-infrared laser power was close to thermal sample damage. In particular, pulse fluencies of about 0.18 J cm^{-2} from FEL [16,32] or OPO [30] were previously used. Not only that high-fluence pulse requirement results in bulky optical sources, but up to 50 K of temperature change [33] will likely lead to sample damage, especially for biological samples.

3.3 THEORY OF CANTILEVER RESONANCE ENHANCEMENT

Our idea of improving photoexpansion sensitivity is to move the IR pulse repetition frequency in resonance with the AFM cantilever resonant mode. In this case, the cantilever ‘integrates’ contributions from many of light pulses, and its response is enhanced by a Q-factor of the cantilever which may be over 5×10^3 in air [34] or above 10^5 in vacuum [35]. This approach requires us to use QCL as the mid-IR source. QCL is electrically pumped semiconductor laser, so its pulse repetition frequency can be adjusted up to MHz range simply by injecting different current pulses.

Behavior of cantilever resonant vibration can be describe by a damped harmonic oscillator model

$$\frac{d^2z}{dt^2} + 2\zeta\omega_0 \frac{dz}{dt} + \omega_0^2 z = \frac{f(t)}{m} \tag{3.2}$$

where $z(t)$ is the deflection amplitude, $\zeta = (2Q)^{-1}$ is the damping coefficient with Q being the quality-factor of the mode, ω_0 is the resonant frequency, $m = k/\omega_0^2$ with k being the force constant of the cantilever when in contact with sample, and $f(t)$ is the applied external force. Since the sample heating and cooling happen in a time scale much shorter than the cantilever response time in our experiments, the expansion force applied to the cantilever may be represented as a train of delta functions

$$f(t) = I_0 \sum_{n=0}^{\infty} \delta(t - nT) \tag{3.3}$$

where $I_0 = \int F_{abs}(t)dt$ is impulse from the absorption-induced mechanical force on the tip and $T = 2\pi / \omega_0$ is laser pulse repetition period. To solve Eq. (3.2), we apply Laplace transform $\mathcal{L}\{...\}$ to both sides and assume $z(0) = 0$, we then obtain

$$z(s) = \frac{I_0}{m} \cdot \frac{1}{s^2 + 2\varsigma\omega_0 s + \omega_0^2} \cdot (1 + e^{-sT} + e^{-2sT} + ...) \tag{3.4}$$

where $z(s) = \mathcal{L}\{z(t)\}$. Next, to know time dependent cantilever deflection $z(t)$, we perform inverse Laplace transform to Eq. (3.4) so

$$z(t) = \mathcal{L}^{-1}\left\{\frac{I_0}{m} \cdot \frac{1}{s^2 + 2\varsigma\omega_0 s + \omega_0^2} \cdot (1 + e^{-sT} + e^{-2sT} + ...)\right\} \tag{3.5}$$

Convolution theorem yields

$$z(t) = \int_0^t L^{-1}\left\{\frac{I_0}{m} \cdot \frac{1}{s^2 + 2\varsigma\omega_0 s + \omega_0^2}\right\} L^{-1}\{(1 + e^{-sT} + e^{-2sT} + ...)\} dt' \tag{3.6}$$

Because

$$\begin{aligned}\mathcal{L}^{-1}\{\frac{1}{s^2+2\varsigma\omega_0 s+\omega_0^2}\} &= \frac{1}{\omega_0\sqrt{1-\varsigma^2}}\cdot e^{-\varsigma\omega_0 t}\sin(\omega_0\sqrt{1-\varsigma^2}t) \\ &\approx \frac{1}{\omega_0}e^{-\varsigma\omega_0 t}\sin(\omega_0 t)\end{aligned} \tag{3.7}$$

and

$$\mathcal{L}^{-1}\{(1+e^{-sT}+e^{-2sT}+\ldots)\} = \sum_{n=0}^{\infty}\delta(t-nT) \tag{3.8}$$

Inserting Eqs. (3.7) and (3.8) into Eq. (3.6) we have

$$z(t) = \frac{I_0}{m\omega_0}\cdot\int_0^t\sum_{n=0}^{\infty}\delta(t'-nT)e^{-\varsigma\omega_0(t-t')}\sin(\omega_0(t\text{-}t'))dt' \tag{3.9}$$

Finally since $\omega_0 T = 2\pi$, the stable equilibrium solution for $t \geq T/\zeta$ is found to be

$$\begin{aligned}z(t) &= \frac{I_0}{m\omega_0}\sin\left(\omega_0 t\right)\sum_{n=0}^{\infty}e^{-\zeta\omega_0(t-nT)} = \frac{1}{T}\frac{I_0}{m\omega_0^2\zeta}\sin\left(\omega_0 t\right) \\ &= \frac{1}{T}\frac{2QI_0}{k}\sin\left(\omega_0 t\right)\end{aligned} \tag{3.10}$$

Equation (3.10) allows us to calculate the amplitude of the cantilever deflection if the period *T*, quality factor *Q*, force constant *k* and initial momentum I_0 are known. Here we give a simple estimation based on the experimental conditions. We usually operate the AFM cantilever at its second bending mode around 200 kHz (*T* = 5 μs), and the Q-factor is experimentally observed to be ~100. The effective force constant *k* can be linked to k_1 using an equivalent point-mass model as described in Ref. [36], where $k_1 = 0.2$ N m^{-1} is

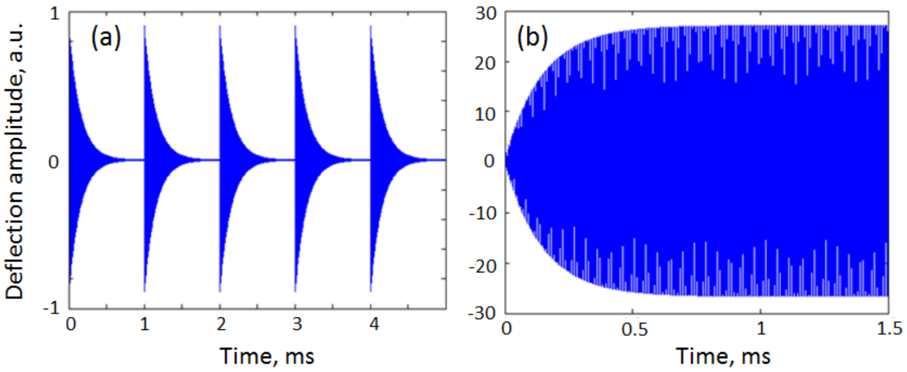

Figure 3.2: Comparing cantilever oscillation at the second bending mode at 200 kHz excited by **(a)** 1 kHz pulses (off resonance) and **(b)** 200 kHz pulses (on resonance).

cantilever's static spring constant. At the second bending mode, we obtain $k/k_c = 40.5$ so $k = 8$ N m^{-1}. Lastly, the initial momentum can be estimated by $I_0 = F_{abs}\tau$, where $\tau = 160$ ns is the laser pulse duration. $F_{abs} = 0.1$ nN is obtained in section 2.2. Combing all these, we finally reach the cantilever deflection amplitude (at tip position) $z = 0.08$ nm.

On the other hand, we can also use Eq. (3.9) to compare the transient oscillation (at 200 kHz) for the resonance enhanced method and the prototype method (with 1 kHz pulses). The calculation results are presented in Fig. 3.2. Note that the deflection amplitude of two figures is of the same arbitrary unit. If one integrates the deflection amplitude over time, the signal in the resonance enhanced method (Fig. 3.2(b)) is about 200 times larger than that in the prototype method (Fig. 3.2(a)). The actual signal of the prototype method should be even smaller because here we assume all the pulse energy goes into the second bending mode of the cantilever, while in reality that mode only get a portion of the pulse energy (see Fig. 3.1(c)). Figure 3.2 (b) also shows that the stable deflection amplitude is established within $2Q$ number of light pulses (~1 ms).

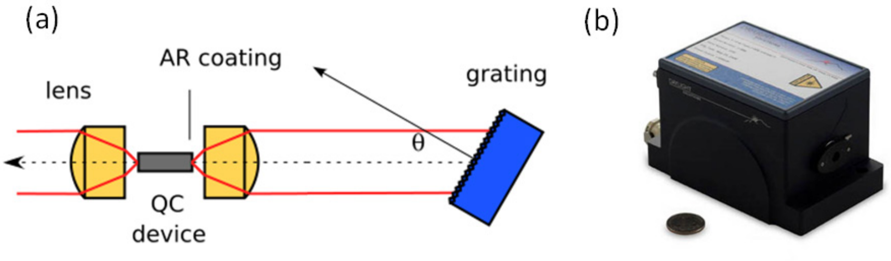

Figure 3.3: External-cavity quantum cascade laser (EC-QCL). **(a)** Schematic of the wavelength tuning mechanism. The external cavity is formed by a diffraction grating and the laser chip. **(b)** A commercial EC-QCL from Daylight Solutions, with its dimension compared to a US quarter. This set of figures was acquired from Daylight Solutions.

3.4 EXPERIMENT

3.4.1 Mid-IR source: tunable Quantum Cascade Laser

QCL is a new type of semiconductor injection laser [37] emitting mid-IR to THz photons. Today, pulsed mode mid-IR QCL routinely operates at room temperature with peak power on the order of watt and requires no external cooling. QCL has superlattice structure, in which IR photons are generated through the intersubband transition of conduction band electrons. The lasing wavelength is determined by the thickness of alternating semiconductor layers and therefore can be precisely engineered.

Special superlattice design can enable QCL with a broadband gain [38–40]. In order to tune the emission wavelength over a wide spectral range for performing spectroscopy, the broad-gain QCL chip is usually coupled with a diffraction grating to form an external optical cavity as shown in Fig. 3.3(a), in the Littrow configuration. The wavelength in the external cavity is selected by the first order diffraction by

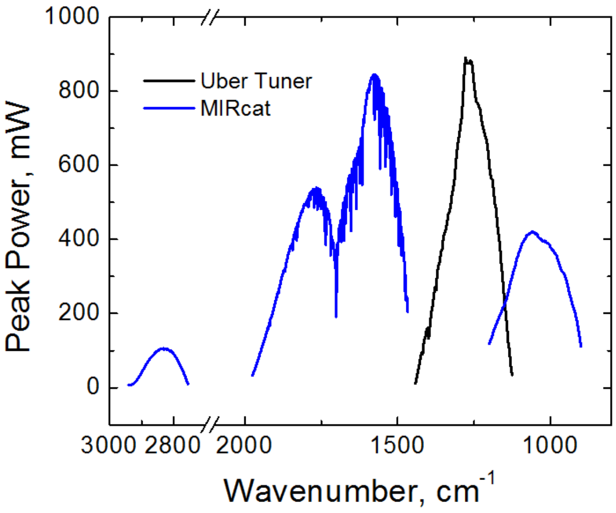

Figure 3.4: Power spectra of two commercial EC-QCLs available in the lab (from Daylight Solutions). MIRcat (blue) has four different QCL chips integrated.

$$\lambda = 2d\sin\theta \tag{3.11}$$

where θ is the angle between the laser beam and the grating normal, d is the grating period. This tuning mechanism requires accurate and stable grating positioning. A single EC-QCL can be tuned up to 15% of its central wavelength [38–40]. By combing multiple QCL chips designed for different wavelength, much wider spectral range is accessible.

In our experiments, two commercial EC-QCLs (Uber Tuner^{TM} and MIRcat^{TM}) from Daylight Solutions are used. They can be operated with 40–1,000 ns pulses and 10–1,000 kHz repetition frequency. The spectral linewidth is about 1 cm^{-1}. Their tuning range and output power are displayed in Fig. 3.4. The sharp power drops in the range of 1500–1800 cm^{-1} is due to water vapor absorption in air [1]. To avoid the effect of strong water absorption on spectral measurement, one could simply choose to skip those wavelengths.

3.4.2 Experimental setup

The goal of this experiment is to demonstrate that high-quality photoexpansion spectra can be obtained under cantilever resonance enhancement with low sample heating induced. We prepared two types of sample. One is spin-coated uniform photoresist polymer films (300 nm-thick SU-8 or LOR), and the other is 50 nm-thick SU-8 patterned in the UT Longhorn shape by e-beam lithography on top of 70 nm-thick LOR film (SU-8 dosage for 50 kV e-beam is 5 μC cm^{-2}). All the samples are on the undoped Si substrate, which has no free-carrier absorption in mid-IR.

Figure 3.5 shows the experimental setup. The EC-QCL was operated with 40 ns light pulses and delivered approximately 100 mW of peak power (pulse energy of 4 nJ) to the sample surface from the bottom of the substrate. The pulse repetition frequency could be varied from 10 to 250 kHz. The beam was focused to a ~100 μm-radius spot using an AR-coated ZnSe lens with 2-inch focus length (not shown). The AFM cantilever (ContGB-G, Budget Sensors) had the first bending mode eigenfrequency of approximately 10 kHz with a Q-factor of ~50 in air and the second bending mode eigenfrequency of approximately 60 kHz with a Q-factor of ~100 in air. In contact with sample, these two resonances are shifted to higher frequencies. The AFM setpoint force was around 10 nN. The sample photoexpansion induced cantilever deflection was picked up by the PSPD and its 'A-B' signal was fed into a lock-in amplifier (Model 7265, Signal Recovery), which was referenced at the QCL pulse repetition frequency. The output of lock-in was *photoexpansion signal*.

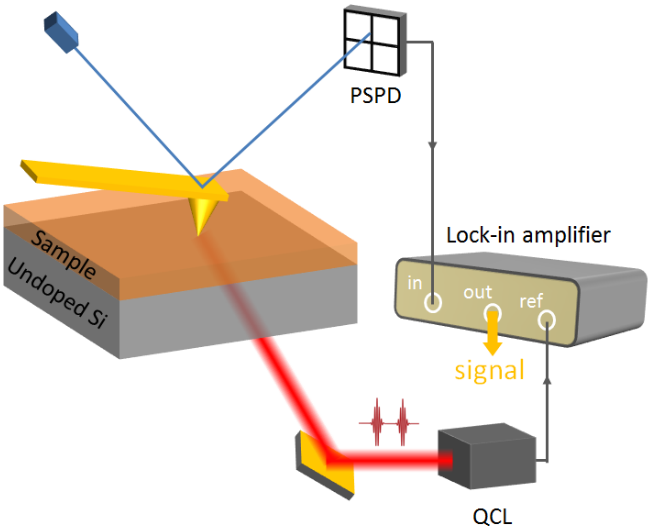

Figure 3.5: Schematic of experimental setup for cantilever resonance enhanced photoexpansion spectroscopy using a tunable mid-IR QCL.

The initial alignment of mid-IR beam to the tip-sample junction could be easily done if a visible tracer is used. Otherwise, one could use a piece of heat sensitive liquid crystal sheet to visualize the mid-IR beam. After the coarse alignment, the beam position was finely optimized by the lens according to the reading on the lock-in.

3.5 RESULTS AND DISCUSSION

Figure 3.6 shows the dependence of the photoexpansion signal on the repetition frequency of QCL pulses. It was obtained by scanning the pulse repetition frequency and recording the respective lock-in output. Two resonant peaks are clearly visible and they correspond to the first two cantilever bending modes. About 100 times enhancement in

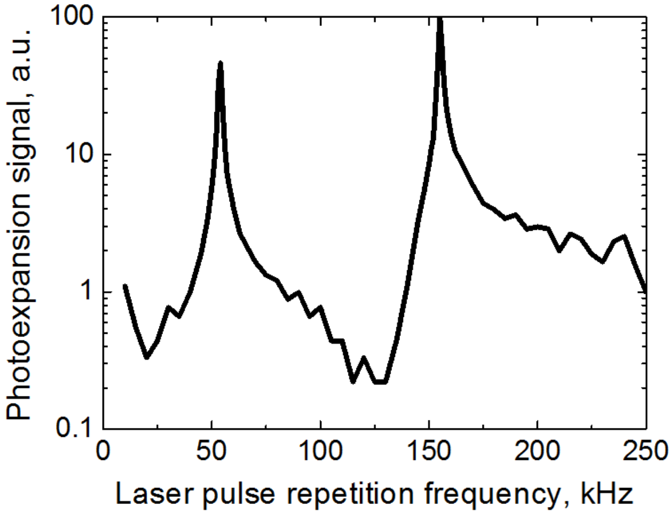

Figure 3.6: The photoexpansion signal recorded as a function of the QCL pulse repetition frequency.

the photoexpansion signal is observed as the repetition frequency of the QCL pulses was tuned to coincide with the second resonant frequency of approximately 155 kHz.

To verify that the enhanced signal in Fig. 3.6 is useful for spectroscopy, we set the repetition frequency of QCL pulses at the high-frequency resonance 155 kHz (for larger Q-factor), tuned the emission wavelengths, and recorded the photoexpansion signal as a function of wavelength to produce photoexpansion spectra. The results are presented in Fig. 3.7 for 300-nm-thick SU-8 (black solid curve) and LOR (red solid curve) polymer films. The data was normalized to the QCL power output at different wavelengths. As we can see, the photoexpansion spectra are in nearly perfect agreement with mid-IR absorption spectra of the same polymers obtained in FTIR (dashed curves). To demonstrate the importance of resonant signal enhancement, next we tuned the repetition

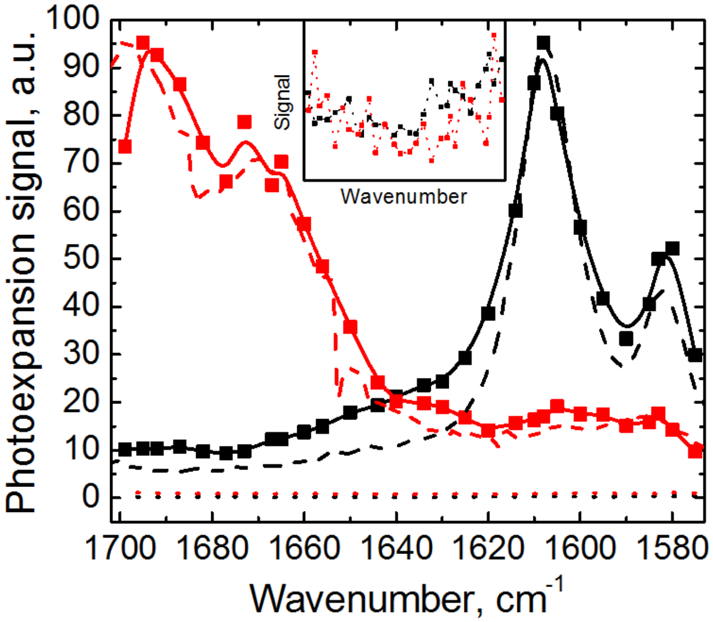

Figure 3.7: Comparing photoexpansion spectra of SU-8 (black) and LOR (red) obtained when the cantilever was on (solid curves) and away from (dotted curves) the cantilever mechanical resonance. Square data points and solid curves are the photoexpansion spectra obtained with the laser repetition frequency set at the AFM cantilever second bending mode of 155 kHz. Dashed curves are the reference absorption spectra measured by FTIR. Dotted curves near zero-level are the photoexpansion spectra obtained with the laser repetition frequency set at 130 kHz, which are also zoomed-in in the inset.

frequency of QCL pulses to 130 kHz (see Fig. 3.6), away from the AFM cantilever mechanical resonances and attempted to record the photoexpansion spectra of the same samples (dotted curves and the inset); in this case the spectral features were indistinguishable from the noise, as shown in the inset of Fig. 3.7.

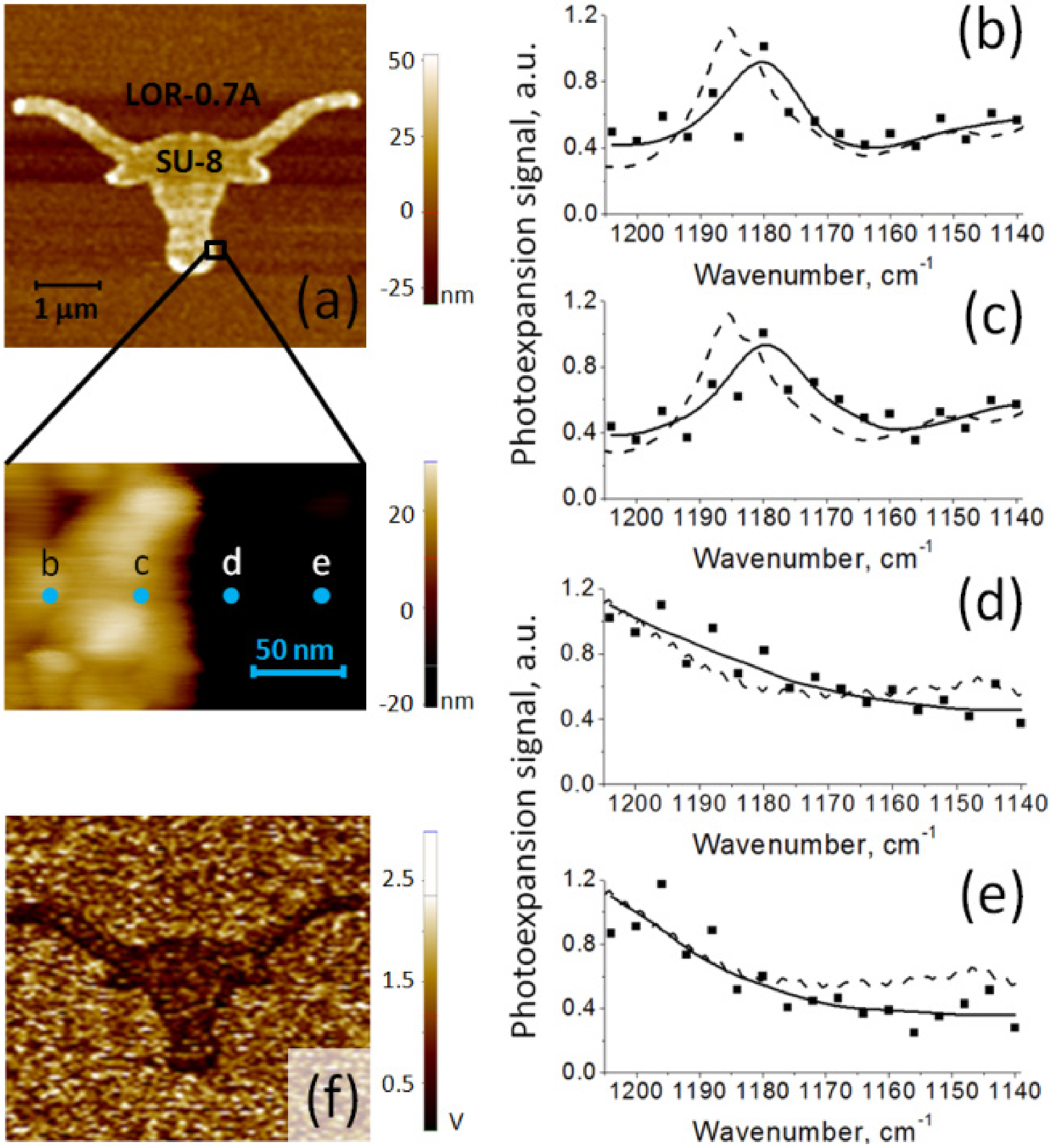

Figure 3.8: **(a)** The AFM topographic image of the 50-nm-thick SU-8 pattern of a Texas Longhorn on top of a 70-nm-thick LOR film on an undoped silicon substrate. Inset: the zoom-in image of the section of the SU-8 pattern with four points marking the positions at which the photoexpansion spectra shown in (b-e) are taken. The separation between the adjacent points is 50 nm. **(b-e)** Photoexpansion spectra (squares are data points, solid lines are for eye guiding) obtained at four sample points shown in (a). Dashed lines are FTIR absorption spectra of SU-8 (b,c) and LOR (d,e). **(f)** Photoexpansion image of Texas Longhorn pattern in (a) taken at laser wavelength of 1204 cm^{-1}. The image size is 128 by 128 pixels, each pixel correspond to a 50-nm-by-50-nm square.

To experimentally demonstrate high spatial resolution, we carried out measurement on the ‘Longhorn sample’. Sample AFM topographic image is displayed in Fig. 3.8(a). We have measured a series of photoexpansion spectra at four points, each separated by a distance of 50 nm from its neighbor as shown in the inset to Fig. 3.8(a). A tunable QCL source operating in the range 1140-1205 cm^{-1} was used to obtain these spectra. The photoexpansion spectra are shown in Figs. 3.8(b-e), along with the FTIR spectra of SU-8 and LOR polymers. The spectra demonstrate that we can clearly distinguish the chemical composition of the SU-8-made Longhorn and the LOR background with better than λ/170 spatial resolution. The data also proves that our technique is capable of measuring spectra from thin samples (50 nm) and is able to identify chemical compounds. Finally, Fig. 3.8(f) shows the ‘photoexpansion IR image’ of the sample obtained by fixing the laser frequency at 1204 cm^{-1} and recording the photoexpansion signal during the AFM scan. As seen in Figs. 3.8(b-e), LOR polymer produces considerably stronger photoexpansion signal than the SU-8 pattern. As a result, the SU-8 pattern appears dark in Fig. 3.8(f).

In this experiment, the sample heating induced by the QCL pulses was extremely low. This estimation is supported by the COMSOL simulation presented in Fig. 3.9. Two types of inhomogeneous samples are simulated with an absorbing compound either positioned on top of (Figs. 3.9(a,b)) or embedded within (Figs. 3.9(c,d)) a non-absorbing compound. The maximum sample temperature increase in both cases is limited to 10 mK. The sample cools down within a few microseconds, before the next QCL pulse arrives. The spatial profile of sample heating in Figs. 3.9 (c,d) also demonstrates high (~50 nm) spatial resolution of this technique, which agrees with the experimental results in Fig. 3.8.

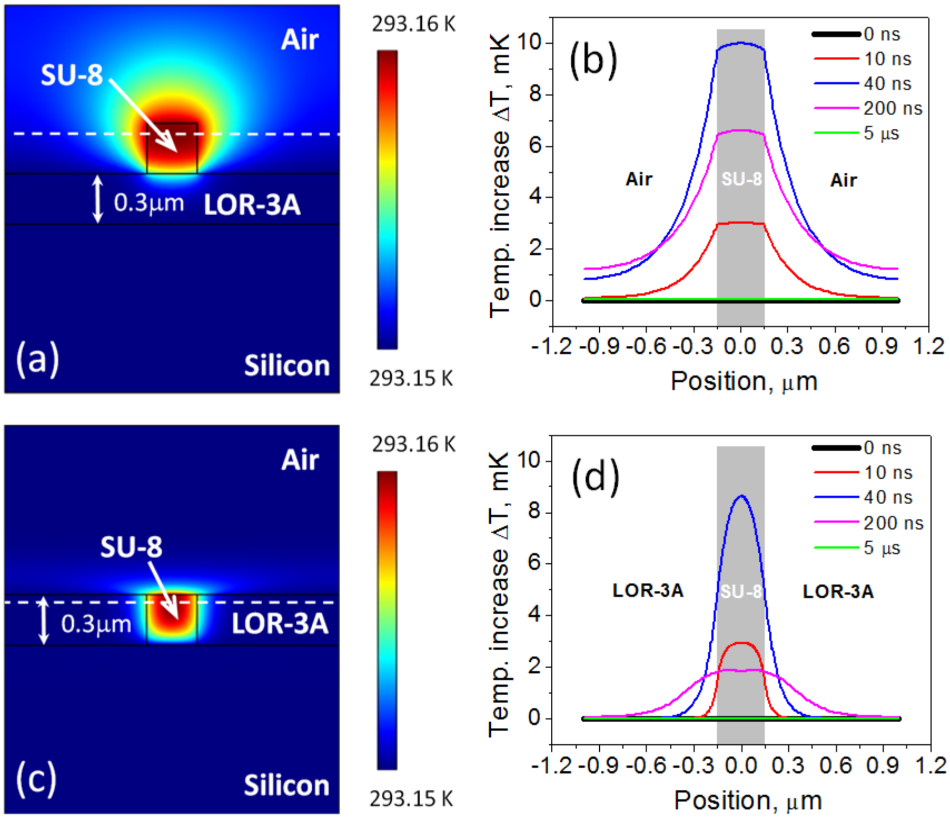

Figure 3.9: Simulations of the temperature distribution in inhomogeneous polymer samples before, during, and after a single laser pulse. The samples are assumed to be illuminated by a 100 mW 40 ns-square pulse, focused to a 100 μm-radius area. **(a)** Temperature distribution at the very end of a laser pulse in a sample consisting of a SU-8 block (300 nm wide and 300 nm thick) placed on top of a 300-nm-thick layer of LOR on a silicon substrate. **(b)** Temperature variation along the dashed line in (a) before (0 ns), during (10 ns), and after (40 ns, 200 ns, and 5 μs) the laser pulse. **(c)** Temperature distribution at the very end of a laser pulse in a sample consisting of a SU-8 block (300 nm wide and 300 nm thick) embedded within a 300-nm-thick layer of LOR on a silicon substrate. **(d)** Temperature variation along the dashed line in (c) before (0 ns), during (10 ns), and after (40 ns, 200 ns, and 5 μs) the laser pulse. The SU-8 parameters are taken from Ref. [20]: thermal conductance $\kappa = 0.3$ W m^{-1} K^{-1}, material density $\rho = 1.2\times10^{3}$ kg m^{-3} and heat capacity $C = 1.2\times10^{3}$ J kg^{-1} K^{-1}; κ, ρ and C for are assumed to be the same for simplicity. The power absorption coefficient is set as 1.7×10^{3} cm^{-1} for SU-8, according to the FTIR measurement at 1180 cm^{-1}. For figure clarity, LOR is assumed to be non-absorbing.

3.6 CONCLUSION

In this chapter, we have demonstrated a technique that allows performing photoexpansion spectroscopy at the nanoscale with low sample heating induced by low-power light sources such as mid-IR QCLs. The approach is based on moving the repetition frequency of laser pulses in resonance with an AFM cantilever bending mode. The experimental setup is extremely simple to implement and operate.

Chapter 4

Tip-Enhanced IR Nano-Spectroscopy on Molecular Monolayer

4.1 INTRODUCTION

One milestone for photoexpansion nano-spectroscopy is to achieve monolayer sensitivity under ambient conditions. With that, this technique can be readily applied to almost any organic sample. In Chapter 3, we enhanced AFM cantilever's responsivity by moving QCL pulses in resonance with the cantilever bending mode. However, there is no much room for further improvement in this direction. As shown previously, Q-factors of the first two cantilever bending modes are 30–100 in air. Although higher Q-factor exists for higher-order resonance [25] and for stiffer cantilever (e.g., quartz tuning fork), the effective spring constant also becomes larger. There is a trade-off between these two factors and experimentally we did not observe much higher photoexpansion signal by operating at higher order cantilever mode or using other commercially available AFM cantilevers. Therefore, to make monolayer expansion detectable, one needs another signal enhancement mechanism.

The strategy is to increase molecules' mid-IR absorption hence thermal expansion with locally enhanced electric field provided by a metallic AFM tip. In this chapter, we show that the field enhancement in the nano-gap between a gold tip and gold substrate is sufficiently strong to produce a detectable monolayer expansion signal, yet without causing thermal damage to the sample. Tip enhancement on the other also improves the

---

Portions of this chapter have been published in Lu, F., Jin, M. & Belkin, M.A. Tip-enhanced infrared nanospectroscopy via molecular expansion force detection, *Nature Photon.* **8**, 307 (2014).

spatial resolution of this technique, which is no longer limited by the thermal diffusion length as in the previous chapter, but only determined by the dimension of 'hot spot' region below the tip.

4.2 TIP ENHANCEMENT IN MID-IR

Here tip enhancement (or tip focusing) refers to lightning rod effect. The AFM tip is coated with a thin layer of gold with thickness greater than the skin depth. Upon p-polarized light (electric field parallel with the tip axis) illumination, free conduction band electrons in the gold layer are polarized to concentrate at the tip apex, hence to form a highly localized field 'hot spot' below the tip. One could also say a strong electric dipole oscillating at the optical frequency is induced inside the tip. This phenomenon is more pronounced at longer wavelength (if not taking into account the local plasmon resonance in the visible range), because the tip becomes effectively sharper and free electrons can 'catch up' the incident field (corresponding to larger negative permittivity).

Figure 4.1(a) shows a three-dimensional COMSOL simulation of tip enhancement at the wavelength λ = 8 μm where the enhancement factor, defined for the light intensity I/I_0, is as high as 1,200. The tip has a half-cone angle of 17° and tip radius of 25 nm. The simulation also indicates the dimension of 'hot spot' is about the same as the tip apex. In this configuration, the photoexpansion force acting on the tip is mainly contributed from the molecules inside the 'hot spot' region which experience much higher heating than the outside molecules. The sample thermal diffusion effect is minimized.

The wavelength dependence of tip enhancement in the mid-IR region is calculated in Fig. 4.1 (b). Generally speaking, the enhancement increases with the wavelength. On

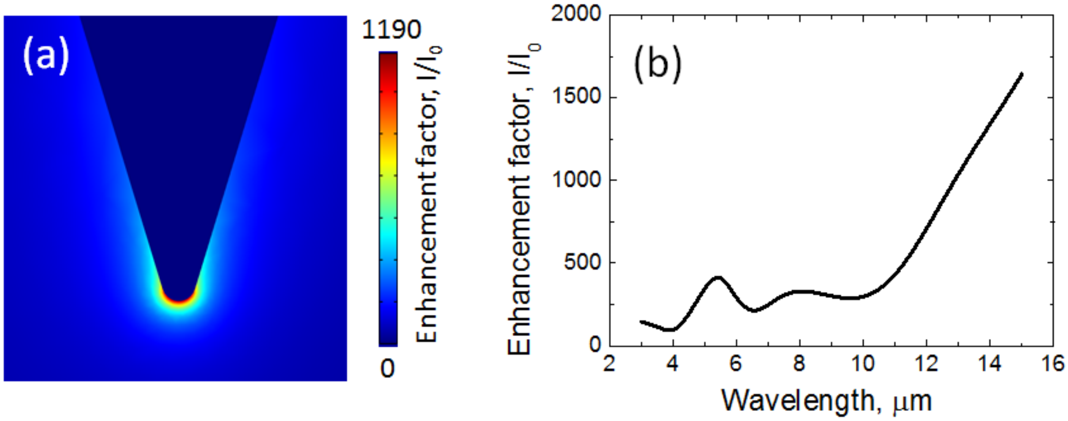

Figure 4.1: Simulation of gold tip enhancement in the mid-IR region. **(a)** Local intensity distribution around the tip at λ = 8 μm. The cone-shaped tip is 10 μm long and light is incident at 75° with respect to the tip axis. Simulation is performed with COMSOL in 3D. **(b)** Enhancement factor (I/I_0) as a function of wavelength. The values in (b) are extracted at the position10 nm below the tip apex.

the other hand, the AFM tip can also be considered as an optical antenna, so at some wavelengths there exist resonant oscillations of electrons [41], which contribute to the peaks shown in Fig. 4.1 (b). Specifically, the fundamental resonance for the tip simulated occurs at λ = 22 μm (not shown), and the peaks at λ = 5.5 μm and 8 μm are the high order resonances. The variation of enhancement in Fig. 4.1(b) needs to be included in spectrum normalization (in addition to laser output power), especially when spectroscopy is performed in a wide spectral range. In this simulation, the tip length is taken to be 10 μm, which is close to the actual length of the illuminated part of the tip in our experiments. This setting is necessary not only for predicting resonant wavelengths, but also because long tip provides more free electrons to contribute to the enhancement.

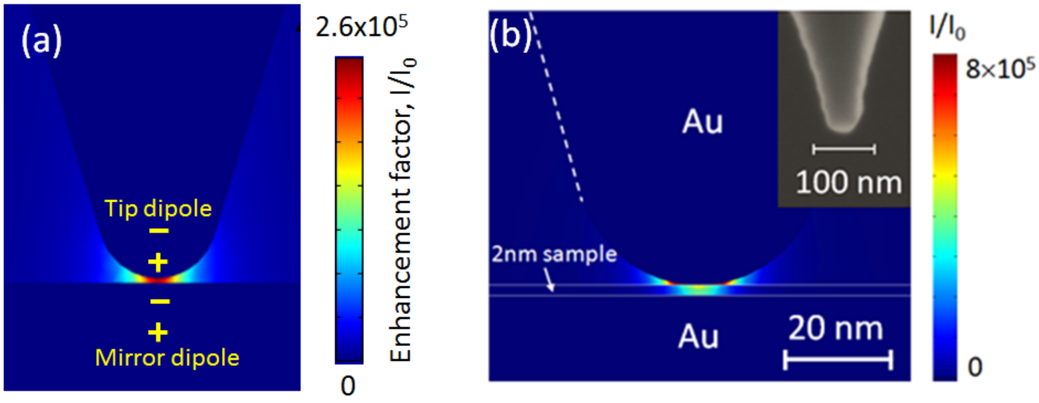

Figure 4.2: Simulation of tip enhancement in a 2-nm gap formed by the gold tip and the gold substrate at $\lambda = 8$ µm. **(a)** The gap is filled with air. **(b)** The gap is filled with an organic monolayer with the refractive index of 1.5 + i0.38. The inset of (b) is a SEM image of an actual tip used in the experiment. The modeling parameters for the tip and incident light are the same as those in Fig. 4.1.

Furthermore, tip enhancement will boost by another two orders in the gap mode as shown in Fig. 4.2. The gap is formed by the gold tip and the gold substrate. The origin of this additional enhancement can be explained with an in-phase mirror dipole in the substrate induced by the tip dipole: when the gap separation is smaller than the tip ‘hot spot’ dimension, the polarization of the mirror dipole dramatically increases, as a result the electric field between the two dipoles is extremely strong. In Fig. 4.2(a) where the separation is only 2 nm (filled with air), the enhancement factor can be as high as 10^5. In this configuration, light that is reflected from the substrate to the tip may also contribute to the high enhancement.

The actual experimental configuration with a monolayer sample is simulated in Fig. 4.2(b). Due to discontinuity of the refractive index, the ‘hot spot’ pattern changes and its dimension inside the monolayer has a diameter of ~10 nm. The simulated tip is compared to an actual tip used in our experiments with its SEM image shown in Fig. 4.2(b).

4.3 MONOLAYER PHOTOEXPANSION

In this section, following the simulation of tip enhancement in Fig. 4.2(b), we deal with monolayer sample heating and thermal expansion based on the experimental conditions. The sample is taken to be 2-nm thick. It is placed on top of a 40-nm-thick layer of gold on top of a 2-µm-thick layer of epoxy (the details of the substrate will be introduced later). The electric field amplitude in the incident mid-IR beam is chosen to correspond to a 100-µm-radius beam spot with 500 mW power in free space. The pulses are 160 ns long and repeated at the frequency of 200 kHz. For general consideration and without loss of much accuracy, the real part of refractive index n and thermal properties of the monolayer are set to be the same as those of a bulk polymer material in Ref. [20].

The imaginary part of refractive index κ for monolayer varies significantly with wavelength. In order to have a typical value of κ for simulation, we focus on the CH_2-wagging mode of EG6-OH molecule. By comparing the strength of different vibrational modes in Ref. [42] and [43], we estimate that the absorption coefficient of the monolayer at CH_2-wagging mode absorption peak is α_{abs} = 6,000 cm^{-1} which corresponds to κ = 0.38.

All the material parameters are summarized in Table 4.1.

Material	$n+i\kappa$ refractive index at 8 µm	k thermal conductivity ($W\ m^{-1}\ K^{-1}$)	ρ density ($kg\ m^{-3}$)	C heat capacity ($J\ kg^{-1}\ K^{-1}$)	α linear thermal expansion coefficient (K^{-1})	v poisson's ratio
monolayer	1.5 + i0.38	0.1	1.2×10^3	1.2×10^3	10^{-4}	0.35
Au	8.5 + i46.4	315	1.93×10^4	0.13×10^3	0.14×10^{-4}	0.42
epoxy	1.5	0.1	1.2×10^3	1.2×10^3	10^{-4}	0.35

Table 4.1: Material parameters for simulating tip enhancement and monolayer heating.

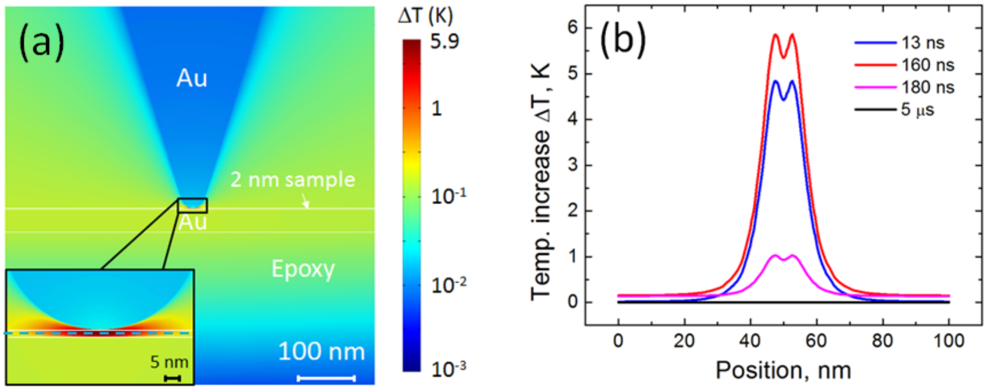

Figure 4.3: Simulation of monolayer sample heating. **(a)** Temperature increase at the end of a 160 ns-long pulse in and around a monolayer sample below the AFM tip. The monolayer is assumed to have an absorption coefficient α_{th} = 6,000 cm^{-1} which corresponds to absorption in PEG and EG6-OH molecules at 1342 cm^{-1} (will be discussed in section 4.4). **(b)** Temperature variation along the blue dash line in (a) during (13 ns, 160 ns) and after (180 ns, 5 μs) the pulse. The sample is cooled to the room temperature before the next pulse arrives (assuming the repetition frequency of laser pulses is 200 kHz)

Figure 4.3(a) presents the simulated temperature distribution in and around the monolayer sample at the end of a 160-ns-long light pulse. Sample heating is estimated to be below 6 K. The low value of simulated sample heating indicates that the spectral measurement should be repeatable over the same sample area without signal degradation. Fig. 4.3(b) plots the temperature increase in the monolayer at different times during and after the laser pulse. The results indicate, in particular, that sample heating and cooling time is much smaller than the laser pulse duration and that the sample maintains the same temperature during most the laser pulse. The spatial resolution in this configuration, if defined as the dimension of hot molecule region, is less than 20 nm.

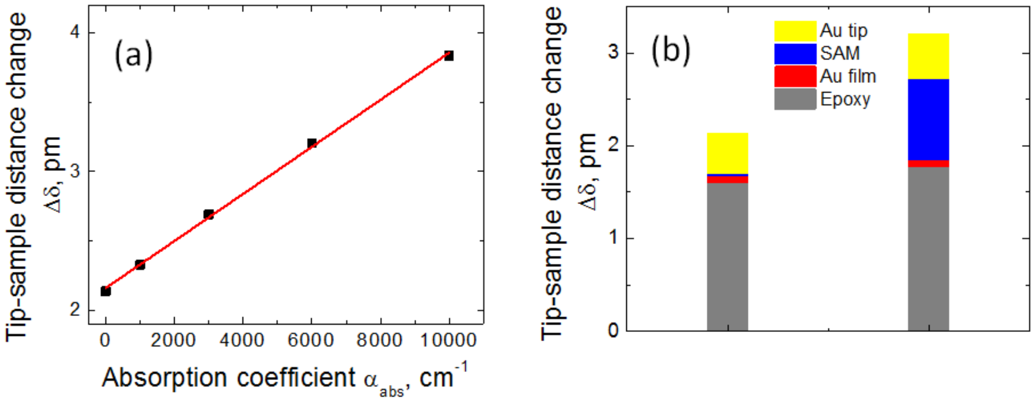

Figure 4.4: Simulation of monolayer sample expansion. **(a)** Dependence of tip-sample distance change Δδ due to sample expansion caused by a mid-IR pulse. **(b)** Histograms showing the accumulated sample expansion from the monolayer, substrate and tip for $\alpha_{abs} = 0\ cm^{-1}$ (left) and $\alpha_{abs} = 6{,}000\ cm^{-1}$ (right). The incident IR pulse was assumed to have a peak power of 500 mW and to be focused to a 100-µm-radius spot for the simulations, similar to the experimental situation.

Next, assuming bulk values of thermal expansion for all materials, we can calculate the laser-induced total tip-sample distance change Δδ and the contributions from each part (monolayer, tip and substrate). The results are shown in Fig. 4.4. We note that Δδ scales linearly with absorption in the monolayer (red line in Fig. 4.4(a)), with a significant background level due to residual light absorption in the gold-coated substrate and the AFM tip (see Fig. 4.3(b)). Because the optical properties of gold are virtually constant in the mid-IR spectral range, the background is expected to be spectrally flat in the measured spectrum.

4.4 EXPERIMENT

4.4.1 Sample preparation

We chose thiolate-bonded self-assembled monolayers (SAMs) as the testing sample, because they have high affinity to the surface of noble metal like gold [44]. Rundqvist, *et al.* [45] reveals that a homogeneous SAM is formed by the growth of sub-monolayer islands first. Sample at this early stage is an excellent candidate for demonstrating high sensitivity and high spatial resolution of tip-enhanced photoexpansion nano-spectroscopy. In order to observe sub-monolayer morphology, the gold substrate itself has to be atomically flat. Direct e-beam deposited gold film has grain structure with the roughness of ~5 nm, which is bad since typical SAM molecules are only 1–5 nm long. Though through annealing, the deposited gold surface can have the atomically flat step-and-terrace structure [4], those substrates need to be stored in a nitrogen environment, as gold is likely to be contaminated quickly by the organic molecules in air. Instead we chose to fabricate the atomically flat template-striped gold (TSG) substrates. Its preparation requires more steps, but the process is highly reproducible and once completed the substrates can be kept in air for more than 6 months, as the gold surface will not be exposed until being used.

TSG were fabricated according to Ref. [46] with some modification. The fabrication process is illustrated in Fig. 4.5. First, the 50 × 75 mm highest-grade V1 mica sheets (Ted Pella) were cleaved and immediately mounted in the chamber of an e-beam evaporation system with fresh facets facing down. A 40 nm-thick gold layer was deposited at the rate of 0.5 Å s^{-1} and a pressure of 8×10^{-6} mbar. The gold-mica sheets

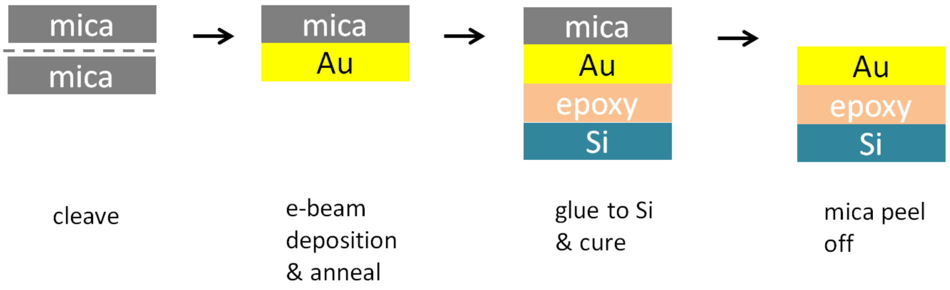

Figure 4.5: Fabrication process of atomically flat template-stripped gold (TSG) substrate.

were then annealed in an oven for 2 h at 300 ^{o}C in a nitrogen environment. The sheets were cleaved into smaller pieces (20 × 20 mm), with the gold surface glued onto silicon pieces of similar size using EPO-TEK 377 (Epoxy Technology), and cured on a hot plate at 150 ^{o}C for 1 h. To expose the gold surface, we simply broke the silicon substrate and carefully peeled the mica by hand. A large surface of gold was routinely obtained with very little mica residue. The conductivity was checked with an ohm-meter. The root-mean-square roughness of the gold surface was measured to be ~3 Å for an area of 5 × 2.5 μm by an AFM in tapping mode. Small holes on the gold films sometimes appeared due to a non-optimized procedure.

On the TSG substrate, three SAM molecules were tested: Hydroxyl-terminated hexa(ethylene glycol) undecanethiol ‘EG6-OH’ (molecular formula: $(HS(CH_2)_{11}(OCH_2CH_2)_6OH$, molecular mass: 468.69 Da) was purchased from Obiter Research; Poly(ethylene glycol) methyl ether thiol ‘PEG’ ($HS(CH_2)_2(OCH_2CH_2)_{21}OCH_3$, 1000 Da) and 4-nitrothiophenol ‘NTP’ ($HSC_6H_4NO_2$, 155.17 Da) were purchased from Sigma-Aldrich. All the materials were used as received.

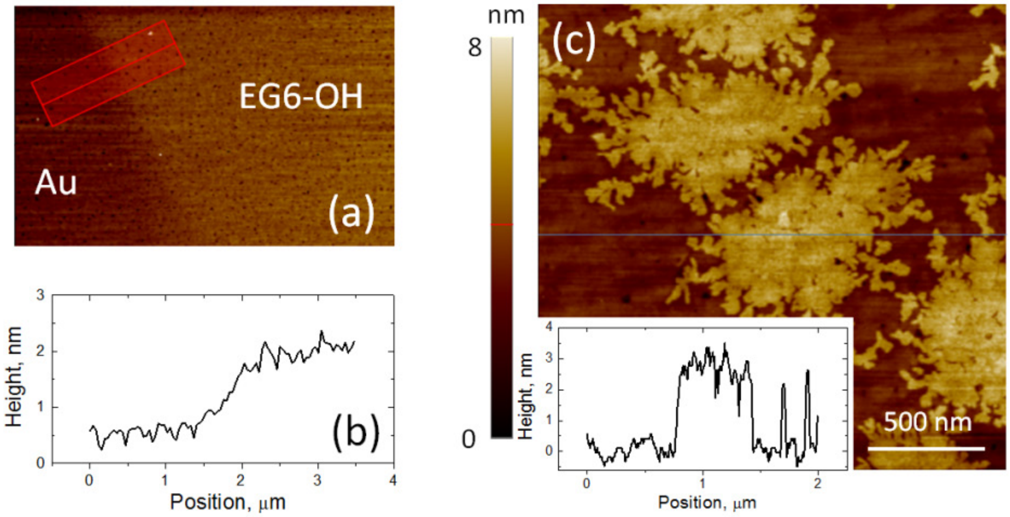

Figure 4.6: Topographic measurement of monolayer samples. **(a)** EG6-OH after partial O_2 plasma etching. The bright regions are EG6-OH monolayer while the dark regions are exposed gold. **(b)** Line-scan averaged within the red box in (a). **(c)** PEG monolayer islands self-assembled on gold after a short immersion time. Inset: line-scan along the blue line.

Among them, EG6-OH and NTP molecules were used to form uniform SAMs, while PEG molecule was used to form sub-monolayer islands. To prepare a uniform SAM sample, the TSG substrate was immersed in a ~1 mM L^{-1} ethanolic solution for 24 h and then rinsed with a copious amount of 200-proof ethanol and dried in a stream of nitrogen gas. To prepare a sub-monolayer island sample, the TSG substrate was immersed in a ~1 mM L^{-1} ethanolic solution for appropriate short periods and then rinsed and dried as above.

Figure 4.6 shows SAM topography on the TSG substrate. To measure the thickness of uniform EG6-OH monolayer, the sample was partially covered by a piece of silicon and exposed to O_2 plasma. Monolayer was removed from part of the sample and then AFM topographic scan was performed across the interface of SAM and exposed gold (see Fig. 4.6(a)). The thickness was measured to be approximately 1.5 nm (see Fig. 4.6(b)). We were not able to measure the thickness of NTP monolayer in this way as its thickness was below the topographic detection level of our system (0.5 nm). NTP thickness was estimated to be substantially smaller than 1 nm. The PEG sub-monolayer islands are clearly seen in Fig. 4.6(c). These islands were growing to connect with each other and their thickness was measured to be 2.5 nm (see the inset of Fig. 4.6(c)). Figure 4.6 also indicates the ultimate flatness of the TSG substrate.

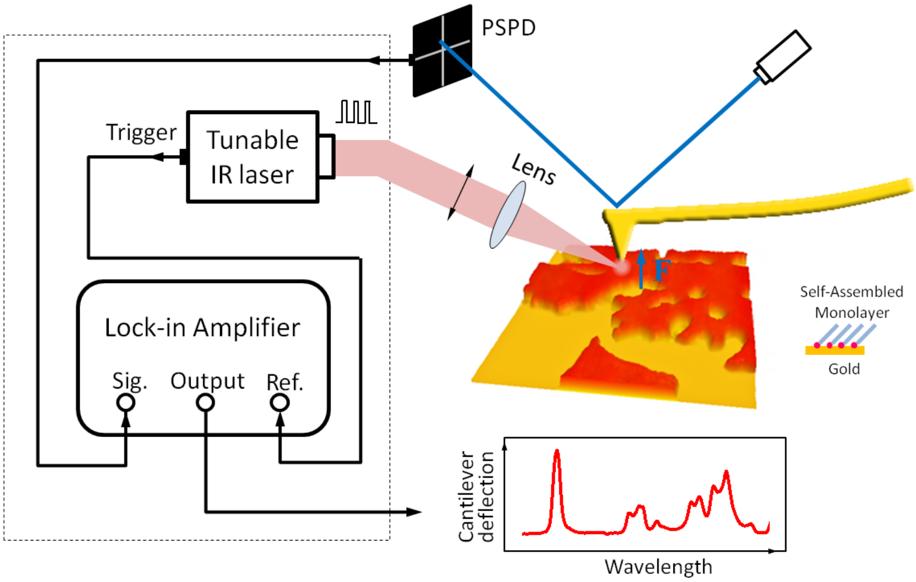
PSPD
Trigger
Tunable IR laser
Lens
F
Lock-in Amplifier
Sig.
Output
Ref.
Self-Assembled Monolayer
Gold
Cantilever deflection
Wavelength

Figure 4.7: Schematic of the experimental setup for tip-enhanced photoexpansion nanospectroscopy on monolayer detection. P-polarized light pulses from a mid-IR laser are focused on a sample. Cantilever deflection due to the molecular expansion force action is detected by a position-sensitive photodetector (PSPD). The PSPD signal is sent to the lock- in amplifier referenced by the laser pulse repetition frequency. The amplifier output is a measure of the cantilever oscillation amplitude at the lock-in reference frequency.

4.4.2 Experimental setup

The setup capable of measuring monolayer photoexpansion is schematically shown in Fig. 4.7. A tunable EC-QCL (Uber Tuner^{TM}, Daylight Solutions) was used as the mid-IR source with its power spectrum measured in Fig. 3.4. Light emission from QCL is inherently polarized along the superlattice growth direction [47]. By proper positioning, p-polarized light pulses were incident onto the sample at 75^{o} with respect to the tip axis. The light pulses were 160 ns long and their petition frequency was carefully maintained to match the second bending mode of the AFM cantilever (ContGB-G, Budget Sensors). Cantilever deflection due to the molecular expansion force action was detected by a PSPD. The PSPD signal was sent to a lock-in amplifier (SR844, Stanford Research Systems) referenced by the laser pulse repetition frequency. The amplifier output was a measure of the cantilever oscillation amplitude at the lock-in reference frequency. The whole system was placed on a vibration isolation stage but there was no acoustic enclosure.

4.5 RESULTS AND DISCUSSION

4.5.1 Nano-spectra of monolayers

The measured photoexpansion spectra on monolayers are displayed in Fig. 4.8 for EG6-OH (a) and NTP (b), respectively. The data were normalized to the QCL light intensity. Figure 4.8 also shows reference absorption spectra (red curves) collected by the mid-IR reflection-absorption spectroscopy (IRAS) for the same monolayer material on gold in Refs. [43,48]. The photoexpansion spectra are in excellent agreement with the absorption spectra, and some vibrational modes of these two molecules are clearly identified. For EG6-OH, the absorption bands centered at 1345 cm^{-1} and 1244 cm^{-1} corresponds to CH_2 wagging and twisting modes, respectively [43]. Owing to the limited tuning range of our QCL source, only part of the stronger C–O–C stretching band (peak at 1130 cm^{-1}) was measured. For NTP molecules, a strong peak around 1339 cm^{-1}, which corresponds to the symmetric NO_2 stretching mode, can be clearly seen. We also observed a much weaker absorption band around 1175~1183 cm^{-1} due to vibration of the benzene ring. The NTP results demonstrate our ability to collect mid-IR spectra from small molecules. On the other hand, the experimental spectra show a flat background

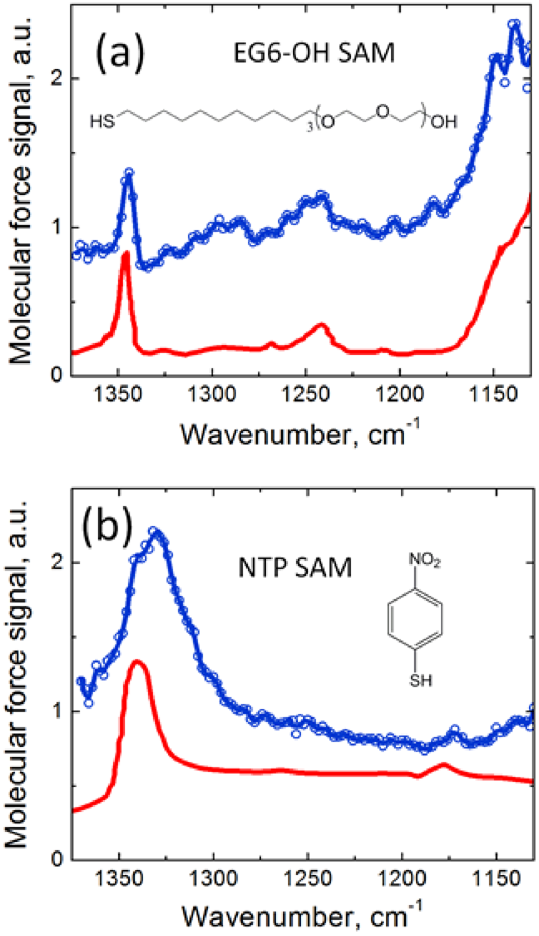

Figure 4.8: Molecular force spectra of self-assembled monolayers on gold. **(a)** EG6-OH. **(b)** NTP. The blue circles are the measured data. The data points are connected by B-splines for eye-guiding. The red curves are the mid-IR reflection-absorption spectra of corresponding SAMs taken from Ref. [43] for (a) and from Ref. [48] for (b). The insets show molecular structure of the samples.

with the signal-to-background ratio at the CH_2 wagging band (Fig. 4.8(a)) to be ~1.7, which is in good agreement with the theoretical prediction of 1.5 obtained from Fig. 4.4. This background issue will be addressed later in Chapter 5.

High spatial resolution is demonstrated with a sample made of monolayer islands of PEG on TSG. PEG molecules have a backbone structure similar to that of EG6-OH with its CH_2 wagging mode peaked at 1342 cm^{-1}. The island height is ~2 nm as confirmed by the topographic measurement in Fig. 4.9(a). Figure 4.9(b) displays a topographic line scan along the blue arrow shown in Fig. 4.9(a). We positioned the AFM tip at different points along the line scan (marked with squares in Fig. 4.9(b)) and collected photoexpansion spectra at these locations. The results are shown in Fig. 4.9(c), where spectra are color-coded and numbered to correspond to the measurement position markers in Fig. 4.9(b). We can distinguish PEG islands from bare gold by monitoring the CH_2 wagging band with a spatial resolution better than 30 nm. Figure 4.9(d) compares the dependence of the cantilever deflection signal along the line scan in Fig. 4.9(b) where the laser frequency is set to the 1342 cm^{-1} absorption line of PEG and to 1352 cm^{-1}, away from the absorption line. As expected, the contrast between PEG and gold is only observed at 1342 cm^{-1}.

The mid-IR chemical mapping capability of PEG islands is demonstrated in Fig. 4.9(e). For this case, we fixed the laser frequency at the PEG absorption peak at 1342 cm^{-1} and recorded the AFM cantilever deflection amplitude as a function of tip position. The mid-IR mapping image shows a clearer contrast and more details, compared to the topographic image of the same sample section shown in Fig. 4.9(a). From the data shown in Fig. 4.9(f) as well as in Figs. 4.9(c,d), we estimate the spatial resolution of our technique to be better than 25 nm, likely limited by the apex size of the AFM tip used in our experiments.

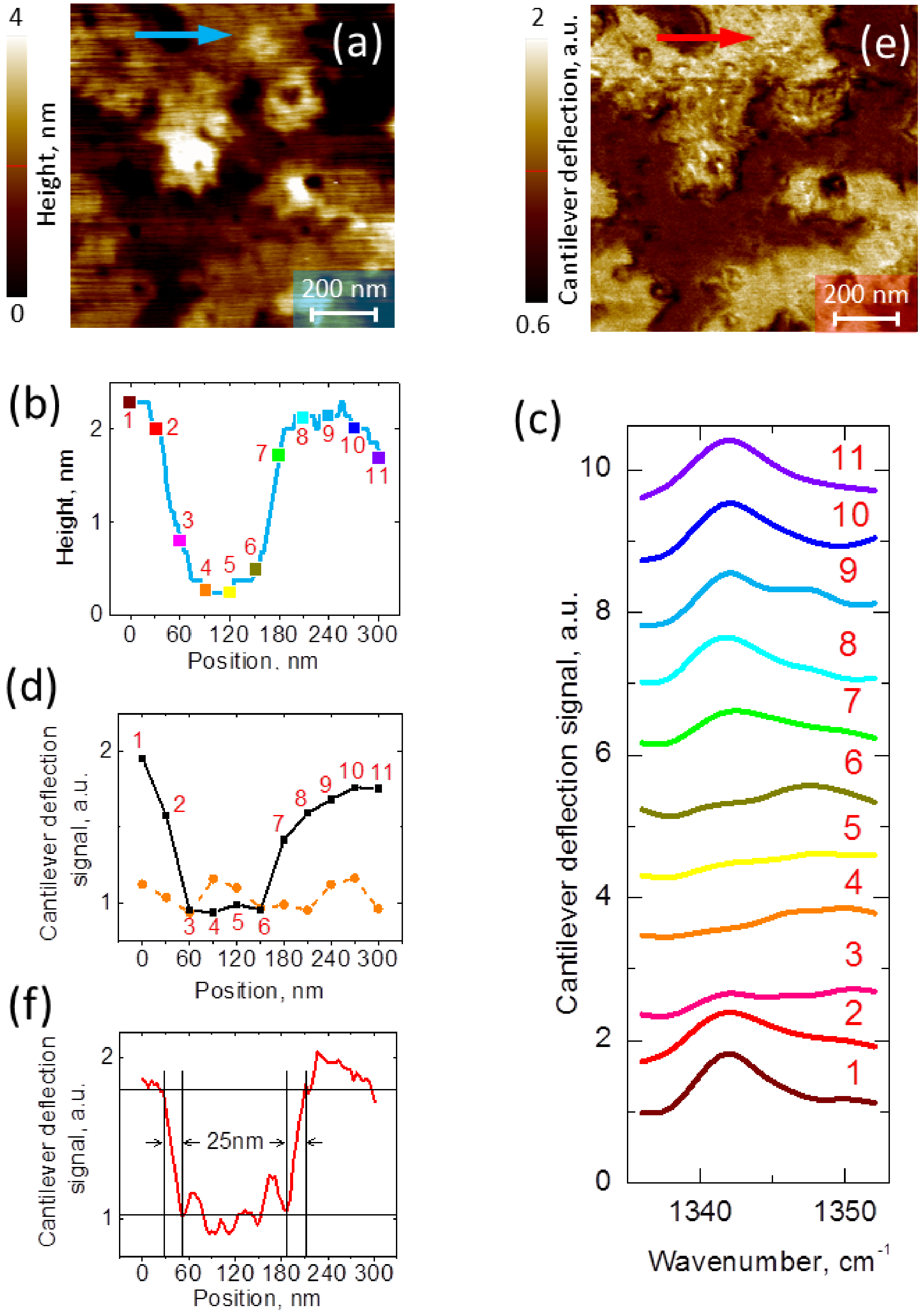
(a)
Height, nm
4
0
200 nm
(e)
Cantilever deflection, a.u.
2
0.6
200 nm
(b)
Height, nm
Position, nm
1
2
3
4
5
6
7
8
9
10
11
0
60
120
180
240
300
(c)
Cantilever deflection signal, a.u.
Wavenumber, cm^{-1}
1340
1350
0
2
4
6
8
10
(d)
Cantilever deflection signal, a.u.
Position, nm
(f)
Cantilever deflection signal, a.u.
Position, nm
25nm

Figure 4.9: Demonstration of spatial resolution. **(a)** Topography of the PEG monolayer islands acquired in contact mode. **(b)** Topographic line scan along the blue arrow in a, showing the height of the monolayer islands to be ~2 nm. Square symbols mark positions where the photoexpansion spectroscopy measurements were performed. **(c)** Mid-infrared photoexpansion spectra taken at the positions indicated in (b). The curves are labelled and colored in accordance with (b). Spectra are offset vertically for clarity. **(d)** Cantilever deflection signal at different points along the topographic scan in (b) for the laser tuned to the 1,342 cm^{-1} PEG absorption line (black squares connected by a black solid line) and to 1,552 cm^{-1}, away from the PEG absorption line (orange circles connect by a dashed orange line). Data points are extracted from spectra in (c). **(e)** Mid-IR mapping of monolayer islands: the lock-in output is recorded as a function of tip position for the mid-infrared laser wavelength fixed at the PEG CH_2 wagging absorption band at 1,342 cm^{-1}. Bright regions are PEG molecules and dark regions are gold. The image has 256 × 256 pixels and was obtained simultaneously with the topographic image in (a). The image was produced by raster scanning at a rate of 0.5 Hz with the lock-in integration time set to 3 ms. The total acquisition time was ~5min. **(f)** Signal along the line scan shown with a red arrow in (e). Data indicate a spatial resolution of ~25 nm for the image in (e).

We estimate that approximately ~300 molecules contribute to cantilever deflection in these experiments. This number is based on the simulated hot-spot diameter of approximately 10 nm (Fig. 4.2(b)) and the molecular density of 4 molecules nm^{-2} [44]. Given signal-to-noise ratio in the spectra shown in Fig. 4.8, we expect to be able to see strong absorption peaks from as few as 30 molecules below the tip.

4.5.2 Cantilever deflection amplitude

Experimentally, we excite cantilever at the second bending mode in contact with the sample. The cantilever deflection amplitude z_2 may be determined from the AC amplitude of the PSPD voltage V_{PSPD} as:

$$z_2 = \frac{V_{PSPD}}{\eta_2} \tag{4.1}$$

where η_2 is the calibration coefficient that links V_{PSPD} with the physical cantilever deflection amplitude z_2.

V_{PSPD} can be determined by direct measurement of the PSPD output with an oscilloscope; it is also linked to the lock-in voltage as $V_{lock-in} = g\,V_{PSPD} \big/ \sqrt{2}$, where g is the lock-in gain coefficient. In our experiments, the maximum V_{PSPD} at the second bending mode was approximately 200 mV.

To determine η_2, we compare the cantilever shape for the first bending mode in free space with the cantilever shape for the second bending mode in contact with sample, see Fig. 2.6. Their amplitudes are adjusted so that the slopes at the cantilever end section are the same. We then know that z_1 cantilever deflection in the first bending mode produces the same PSPD signal as the second bending mode with $z_2 \approx z_1/35$ deflection. The calibration between z_1 and V_{PSPD} can be obtained through the force-distance curve measurement on a hard surface as discussed in section 2.3. Such measurement gave us $V_{PSPD} = 23\ \mathrm{mV\ nm^{-1}} \times z_1$.

Putting things together, we have

$$z_2 = \frac{200\ \mathrm{mV}}{35 \times 23\ \mathrm{mV \cdot nm^{-1}}} \approx 0.25\ \mathrm{nm}$$

The theoretical value of z_2 can be calculated using Eq. (3.10) which simplifies the cantilever as a harmonic oscillator. We use $\tau = 160$ ns, $T = 5$ µs, experimentally-measured $Q = 93$ and $k = 8\ \mathrm{N\ m^{-1}}$ (derived in section 3.3), but still need to find out the value of photoexpansion force F_{abs} in our experiments. To do that, we first calculate the tip indentation δ via Eq. (2.1). The values of reduced Young's modulus E^* and adhesion force $F(a_0)$ for our monolayer samples are assumed to be the same as those measured in Ref. [49] for the $CH_3(CH_2)_{17}SH$ monolayer sample: $E^* = 5$ GPa and $F(a_0) = 10$ nN. The assumption is reasonable because the tip radius used in our experiments (~25 nm) is similar to that used in Ref. [49] (~20 nm). Equation (2.1) then gives the sample indentation of $\delta \approx 0.7$ nm for the contact mode setpoint force $F = 10$ nN used in our experiments. Next, the total tip-sample distance change is calculated to be $\Delta\delta \approx 3.2$ pm in Fig. 4.4, which corresponds to CH_2 wagging mode of EG6-OH molecule with the absorption coefficient $\alpha_{abs} = 6{,}000$ cm^{-1}. With all the parameters known in Eq. (2.2), $F_{abs} = 0.13$ nN is obtained. Inset it to Eq. (3.10), we have $z_2 = 0.1$ nm, which is close to the experimentally-measured $z_2 \approx 0.25$ nm. The discrepancy between theory and experiment is likely stemming from uncertainty in the temperature change and photoexpansion of the sample as well as in the Young's modulus of the sample.

Besides F_{abs}, electromagnetic forces may also affect cantilever deflection [50]. We evaluated the optical force on the tip in COMSOL using Maxwell's stress tensor for experimental conditions with 500 mW laser power focused onto a 100-μm-radius spot below the tip (cf. Fig. 4.2(b)). We obtained $F_{opt} \approx 0.3$ pN $\ll F_{abs}$. We also note that, unlike F_{abs}, F_{opt} is virtually independent of the absorption coefficient of the monolayer film. Thus, it is the mechanical force action on the AFM tip that produces spectral signatures in our experiments.

4.5.3 Spectrum normalization

The cantilever deflection signal output by the lock-in should be normalized by the local light intensity which equals laser output power (Fig. 3.4) times tip enhancement factor (Fig. 4.1(b)). This principle was implemented alternatively in our experiments that

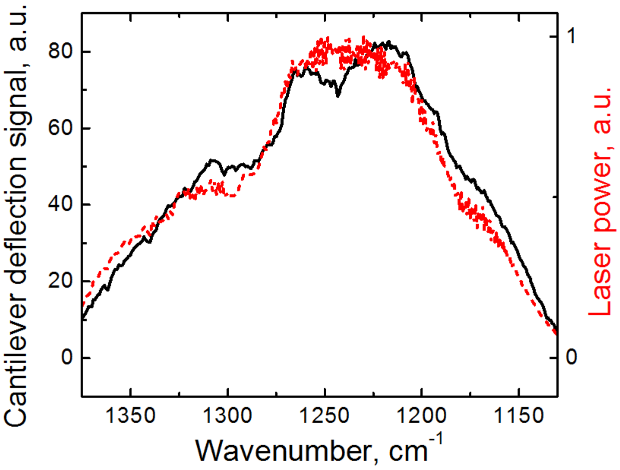

Figure 4.10: Comparison of the background TSG spectrum (black) with the QCL power spectra taken by a MCT detector (red).

the measured sample spectra were normalized by the spectrum taken on a clean TSG substrate. The photoexpansion signal on TSG substrate originates from the expansion of the substrate and the AFM tip due to residual broadband absorption of mid-IR light by gold (see Fig. 4.4 in the case of $\alpha_{abs} = 0$ cm^{-1}). This normalization approach was verified in Fig. 4.10 where the spectrum on a TSG substrate (black curve) agreed with the laser power spectrum measured by a mercury cadmium telluride (MCT) detector (red curve). Note that the variation of enhancement factor in the spectral range of 1130–1370 cm^{-1} is small (cf. Fig. 4.1(b)).

This approach can also help to overcome the beam steering issue. In some EC-QCLs, the laser beam is emitted to slightly different directions at different wavelengths. As a result, the power spectrum received by AFM tip is not the same as the original power spectrum. Because cantilever deflection on a substrate only responds to the local light intensity below the tip, it is more accurate to do the normalization with the substrate spectrum if beam steering is an issue.

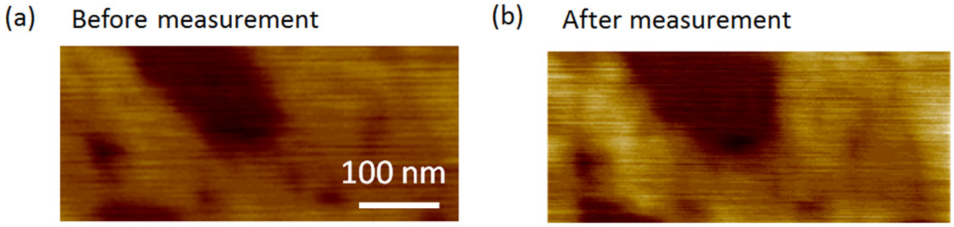

Figure 4.11: AFM topography scanning on PEG sub-monolayer islands sample before **(a)** and after **(b)** photoexpansion measurement carried out in Fig. 4.9.

4.5.4 Sample damage

Since monolayer heating is estimated to be below 6 K, it is unlikely to cause thermal damage to the sample. After performing all the photoexpansion measurement described in Fig. 4.9 on the PEG sample, we scanned the topography of the same sample area. The result is shown in Fig. 4.11. No damage was observed.

4.6 CONCLUSION

We have demonstrated that mid-IR vibrational spectra of molecular monolayers and monolayer islands could be collected under ambient conditions with high sensitivity and better than 25 nm spatial resolution by detecting the mechanical force exerted on an AFM tip by molecules excited with pulses of mid-IR radiation. Approximately 300 molecules are interacting with the AFM tip in our experiments, and the set-up sensitivity is estimated to be ~30 molecules. Mid-IR spectra obtained by detecting mechanical molecular action show higher sensitivity than those obtained by the best s-NSOM systems [4,5] applied to similar or thicker samples.

Chapter 5

Photoexpansion Background Suppression with Two QCLs

5.1 INTRODUCTION

In Chapter 4 we performed photoexpansion nano-spectroscopy on molecular monolayers by employing optical enhancement of metalized AFM tip as well as mechanical enhancement of cantilever resonance. The spectra shown in Figs. 4.9 and 4.10 contain contributions from approximately 300 molecules under the AFM tip. This sensitivity may potentially be further improved to the single-molecule level, if one could suppress the high background presented in those spectra. The background signal, as analyzed in Fig. 4.4, comes from the light absorption and expansion by the gold substrate and gold tip.

Our principle of suppressing background signal is to remove its periodicity from the laser pulse repetition frequency, as this is the frequency at which the cantilever deflection signal is extracted from the lock-in amplifier. We implement our strategy by using a second QCL ("suppression laser"). The wavelength of the suppression laser is set to be away from any sample absorption band, so it only induces background photoexpansion of the substrate and tip, but not of the sample. By turning on the suppression laser in proper ways, the Fourier component of cantilever deflection signal at the laser pulse repetition frequency will only contain the contribution from the monolayer expansion.

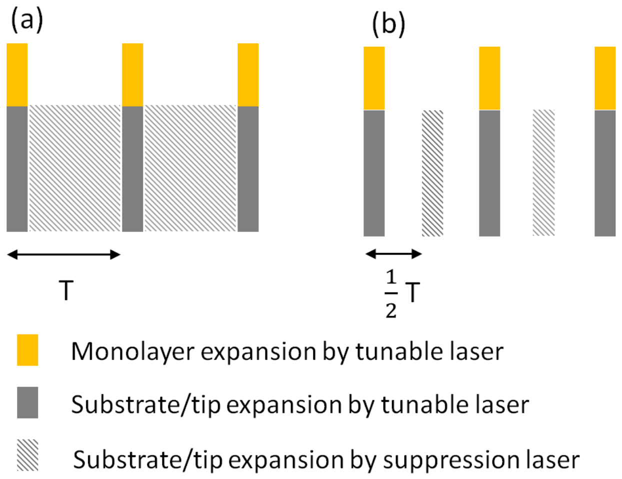
(a)
(b)
T
$\frac{1}{2}$T
Monolayer expansion by tunable laser
Substrate/tip expansion by tunable laser
Substrate/tip expansion by suppression laser

Figure 5.1: Two schemes of background suppression using two QCLs. **(a)** The suppression laser is operated in nearly cw mode **(b)** The suppression laser is operated in pulsed mode. The repetition frequency is same as that of the tunable laser, but two pulse trains have π phase delay.

5.2 EXPERIMENT

We propose two schemes of using suppression laser to remove background signal. In the first scheme, the suppression laser is operated nearly continuous-wave and being turned off only for a short moments in time when the other tunable laser is on, as illustrated in Fig. 5.1(a). For this case, the substrate and tip are continuously heated, while the monolayer sample only absorbs energy and is being heated up when the emission wavelength of the tunable laser overlaps with sample absorption bands. As a result, the periodic variation of expansion is purely from the sample and is extracted by the lock-in. However due to heat buildup inside the QCL chip for high duty-cycle operation, the laser output power cannot be maintained at a constant level. So this scheme is not easy to be implemented.

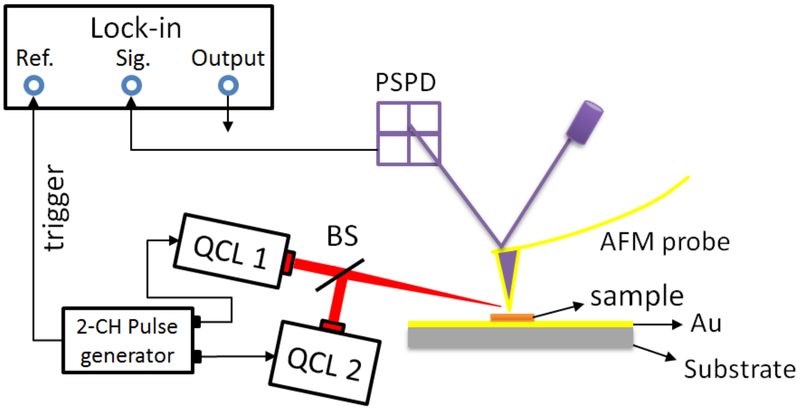

Figure 5.2: Schematic of the experimental setup for background-free photoexpansion nano-spectroscopy. QCL1 is the tunable laser and QCL2 is the suppression laser whose wavelength is fixed away from any sample absorption band. Two QCLs have the same pulse repetition frequency, by which the lock-in amplified is referenced. BS: beam splitter.

The second scheme employs the suppression laser being operated in pulsed mode with the pulse width and repetition frequency being the same as those of the tunable laser. The delay between the pulses of the suppression laser and the tunable laser is set to be half of the period, as illustrated in Fig. 5.1(b). The power of two lasers is balanced so that they will induce the same background signal. For this case, the Fourier component of the photoexpansion force on the AFM cantilever at the laser pulse repetition frequency will only contain the contribution from the sample photoexpansion as shown in Fig. 5.1(b).

We tested the second scheme on the experimental setup shown in Fig. 5.2. Two identical electrical pulse trains with π phase delay were generated by a two-channel function generator (Teledyne Lecroy) and were used to drive two QCLs (Über Tuner^{TM} and MIRcat^{TM}, Daylight solutions). The laser beams were combined through a beam splitter and first focused onto a fast photodetector (PVM-10.6, time constant < 1 ns, Boston Electronics) that was placed at the tip position. The output signal of the photodetector was monitored on an oscilloscope, from which we confirmed that the two laser pulses indeed had the same pulse width and repetition frequency, and were delayed by half of the period. We finely optimized the beam overlap according to the signal on the photodetector. After that, the photodetector was removed and we proceeded to measure the sample. The laser pulses have width of 160 ns and their repetition frequency was carefully maintained at the second bending of the AFM cantilever (ContGB-G, Budget Sensors) at ~200 kHz, at which the cantilever deflection signal was extracted from the lock-in amplifier (SR844, Stanford Research Systems).

5.3 RESULTS AND DISCUSSION

Prior to collect the monolayer spectrum, a power calibration for the two QCLs was needed. This was to make sure that at each wavelength of the tunable laser, the pulses from the two QCLs would induce same amount of heat to the gold substrate and tip. The calibration was performed on a clean TSG substrate, with one representative result plotted in Fig. 5.3, in which we recorded the cantilever response on the lock-in as a function of the power of the tunable laser. (The power of the suppression laser is fixed.) The left-most data point corresponded to below-threshold operation of the tunable laser, so the lock-in output of 26 a.u. was due to the photoexpansion force induced by the suppression laser alone. With the increased power of the tunable laser, the lock-in signal reached a minimum of 2 a.u.. In this case, the gold substrate and tip were thermally

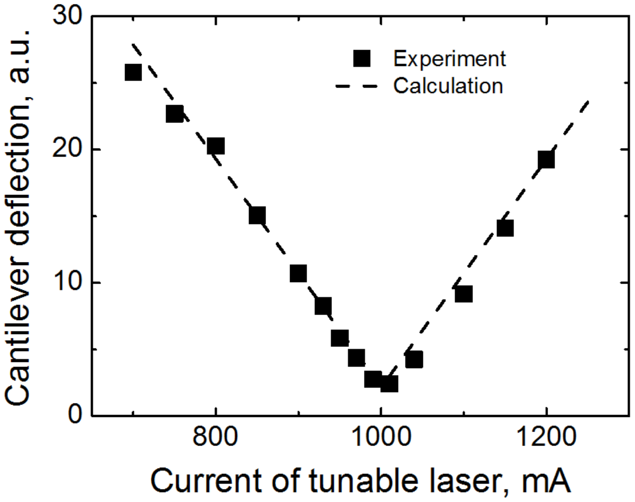

Figure 5.3: Cantilever signal recorded by lock-in as a function of the tunable laser power. The power was tuned via injecting different current. The power of the suppression laser was fixed. The dashed line is the calculated performance using Eq. (5.2) with $D = 0.5$.

expanding with the same amplitude at the second harmonic frequency of lock-in reference. The balanced power setting at this data point was saved for the future use on monolayer spectrum collection. Such calibration was carried out for each wavelength of the tunable laser.

The necessity for delaying the two laser pulses by half of the period was justified in Fig. 5.4. In this measurement (also on the TSG substrate), we used the balanced power settings previously acquired in Fig. 5.3 so when the delay was exactly half of the period, the lock-in signal reached a minimum of 3 a.u.. With the delay deviated from half of the period, the lock-in signal increased, which means the photoexpansion force had more and more Fourier component at the lock-in reference frequency. The lock-in output a maximum signal of 60 a.u. when the two laser pulses overlapped.

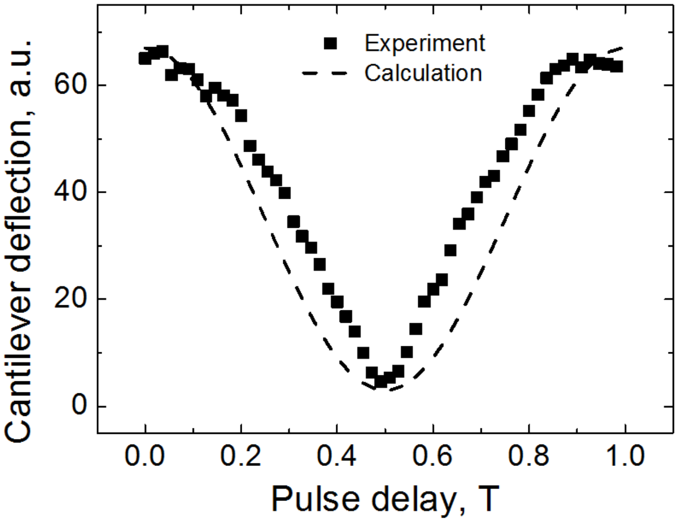

Figure 5.4: Cantilever signal recorded by lock-in as a function of the phase delay between two laser pulses. The dashed line is the calculated performance using Eq. (5.2) with $a = b$.

The behavior captured in Figs. 5.3 and 5.4 can be explained with a simplified model, in which the light pulses from the two QCLs are represented by an impulse train

$$f(t) = \sum_{P \in Z} (a \cdot \delta(t - PT) + b \cdot \delta(t - (P + D)T)) \tag{5.1}$$

where a and b stands for the power of the tunable laser and suppression laser, respectively. T is the pulse period and D is the delay between two pulses. The Fourier coefficient of Eq. (5.1) at the frequency $\omega = 2\pi/T$ is found to be

$$S_\omega = a + be^{-i2\pi D} \tag{5.2}$$

which represents the cantilever signal extracted from the lock-in. In Fig. 5.3, $D = 0.5$, so we have $S = a - b$. While in Fig. 5.4, $a = b$, so we have $S = 1 + e^{-i2\pi D}$. These two

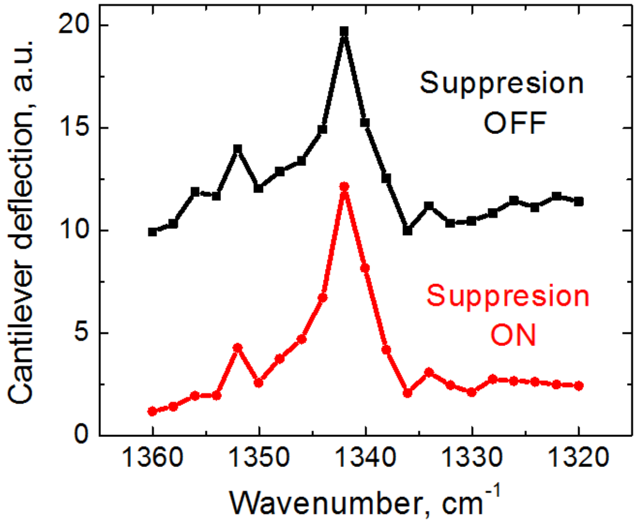

Figure 5.5: PEG monolayer spectrum acquired with (red) and without (black) the use of the suppression laser. The peak at 1342 cm^{-1} corresponds to the CH_2 wagging mode.

expressions are plotted as the dashed curves in the respective figure, which have a good agreement with the experimental data.

Lastly, we proceeded to the spectral measurement on the PEG monolayer. The sample preparation was described in section 4.4. PEG molecules have an absorption band around 1342 cm^{-1}, corresponding to the CH_2 wagging mode on its glycerine backbone. The measured photoexpansion spectra are shown in Fig. 5.5. First, we collected the spectrum with the tunable laser alone (black curve), the signal-to-background ratio in this case turned out to be 2. The spectrum was then re-taken with the suppression laser applying the previously saved balanced power settings for each wavelength. As expected, the result (red curve) shows that the background was reduced, and the signal-to-background ratio was improved to be 6.

5.4 CONCLUSION

We have demonstrated that the background signal presented in the monolayer photoexpansion spectra, which is due to mid-IR absorption by the substrate and tip, can be suppressed using two QCLs. The key is to remove the Fourier component of the background signal from the lock-in frequency. This method is useful for the future demonstration of higher detection sensitivity of photoexpansion measurement.

Chapter 6

Heterodyne Detection of Photoexpanison Force

6.1 INTRODUCTION

In the previous chapters, the photoexpansion force F_T we discussed is the first-order approximation of the tip-sample interaction force. The expression of F_T is given by Eq. (2.2) which indicates F_T is proportional to sample's light absorption. This assumption was justified by comparing sample photoexpansion spectra to their FTIR absorption spectra with a good agreement (e.g. Figs. 3.7 and 4.10), and was also justified by the simulation in Fig. 4.4(a).

The second-order approximation term of the interaction force has been paid little attention. It represents the nonlinear interaction between tip and sample, through which the sample absorption information can also be extracted. To explore that, one needs to oscillate the tip at a frequency different from the laser pulse repetition frequency. In this case, the tip-sample distance change will have contributions from both the tip position change and the sample photoexpansion, so that through the quadratic interaction a new force component at the heterodyne frequency will be generated. The concept has been similarly implemented in the nonlinear ultrasonic force microscopy [51–55] and scanning near-field ultrasound holography [56–58], in which the tip and the sample are vibrated at different ultrasonic frequencies.

In this chapter, we explore the resonant heterodyne photoexpansion force. By carefully choosing the laser pulse repetition frequency and the tip oscillation frequency so that their difference (or sum) matches a cantilever resonant mode, the cantilever deflection due to heterodyne force action will be amplified by the cantilever's Q-factor. We will demonstrate that the sample photoexpansion spectra obtained from heterodyne detection have the comparable signal-to-noise ratio and amplitude with those obtained in the previous chapters.

6.2 THEORY

To efficiently generate a heterodyne force component, it requires the tip-sample interaction maintained on the nonlinear curve plotted in Fig. 6.1 (black curve). Because this short-distance interaction only spans over ~1 nm, it is better to operate AFM in the contact mode rather than the tapping mode, as the tapping amplitude is usually > 10 nm.

To understand the frequency mixing process, one can expand the tip-sample interaction force $F(z)$ in a power series around the equilibrium position z_0

$$F(z) = F(z_0) + \Delta\delta \cdot F'(z_0) + \frac{\Delta\delta^2}{2} \cdot F''(z_0) + \ldots \qquad (6.1)$$

where $\Delta\delta = z - z_0$ stands for the tip-sample distance change. The first term on the right-hand side of Eq. (6.1) stands for the setpoint force in AFM contact mode. In the experiments, we usually take it to be ~ 10 nN. The second term has a linear dependence on $\Delta\delta$, and it represents the conventional photoexpansion force discussed in the previous chapters [16–18], which is repeated at the laser pulse repetition frequency. Its magnitude is on the order of ~ 100 pN (see section 2.2). The third term which depends quadratically on $\Delta\delta$ is the source for the heterodyne force. Provided that $\Delta\delta$ is a linear combination of the piezo-driven tip oscillation Δz_{tip} at frequency ω_p and the local sample expansion Δz_{sample} at pulse repetition frequency ω_l

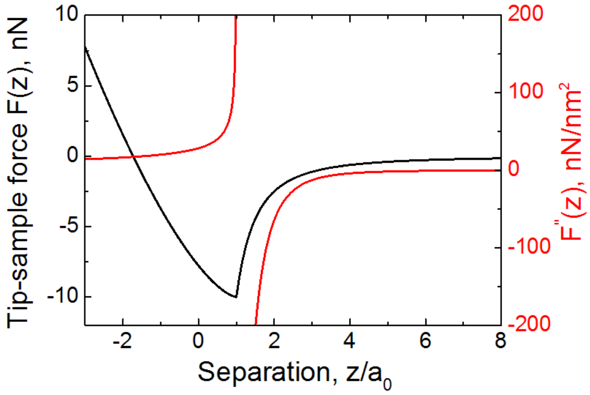

Figure 6.1: The dependence of tip-sample interaction force $F(z)$ (black curve) and heterodyne coefficient $F''(z)$ (red curve) on the tip-sample separation z. The curves are plotted using Eq. (2.1) with the parameters: effective intermolecular distance $a_0 = 0.24$ nm, Hamaker's constant $H = 14 \times 10^{-20}$ J, tip radius $R = 25$ nm, and reduced Young's modulus $E^* = 3$ GPa.

$$\Delta\delta = \Delta z_{\text{tip}} e^{-i\omega_p t} + \Delta z_{\text{sample}} e^{-i\omega_l t} + c.c. \tag{6.2}$$

The third term of Eq. (6.1) becomes

$$\begin{aligned}\frac{\Delta\delta^2}{2}\cdot F''(z_0) = \frac{1}{2}F''(z_0)\cdot(&\Delta z_{\text{sample}}^2 + \Delta z_{\text{tip}}^2 + \Delta z_{\text{sample}}^2 e^{-i2\omega_p t} + \Delta z_{\text{tip}}^2 e^{-i2\omega_l t} \\ &+2\Delta z_{\text{sample}}\Delta z_{\text{tip}} e^{-i(\omega_p \pm \omega_l)t} + c.c.)\end{aligned} \tag{6.3}$$

From Eq. (6.3), we find the heterodyne force to be

$$F_{\text{het}}(z_0) = F''(z_0)\Delta z_{\text{sample}}\Delta z_{\text{tip}} e^{-i(\omega_p \pm \omega_l)t} \tag{6.4}$$

Eq. (6.4) indicates that the heterodyne force is proportional to the sample light absorption, and in principle can be amplified by the tip oscillation amplitude (heterodyne amplification).

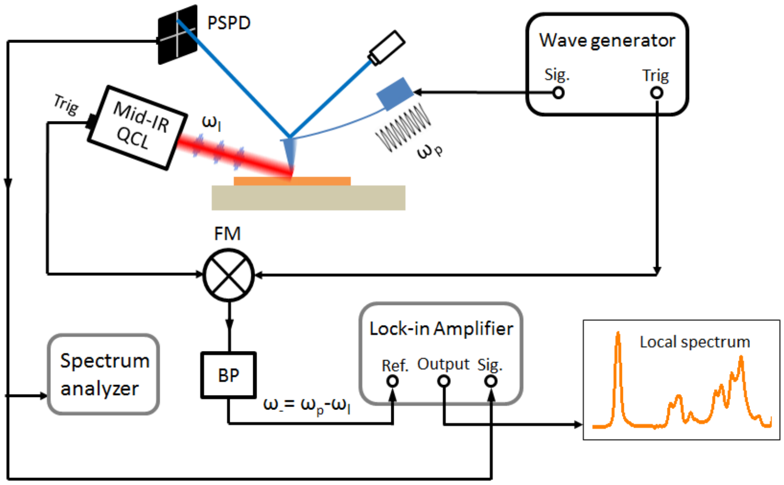
PSPD
Wave generator
Sig.
Trig
Trig
Mid-IR QCL
ω_l
ω_p
FM
Lock-in Amplifier
Ref.
Output
Sig.
Local spectrum
Spectrum analyzer
BP
$\omega_- = \omega_p - \omega_l$

Figure 6.2: Schematic of the experimental setup for photoexpasion nano-spectroscopy with heterodyne detection. The lock-in amplified is referenced at the difference frequency of laser pulse repetition and tip oscillation. FM: frequency mixer, BP: band pass filter.

6.3 EXPERIMENT

Heterodyne detection of sample photoexpansion was investigated on the setup shown in Fig. 6.2. The AFM was operated in contact mode. After initial approach (setpoint force ~10 nN), the cantilever (ContGB-G, Budget Sensors) was oscillated by the bimorph piezo with sinusoidal voltage applied from a function generator (Rigol). At the same time, the sample was illuminated by light pulses from an EC-QCL (Uber Tuner^{TM}, Daylight Solutions). The cantilever deflection was monitored by a position-sensitive photodetector (PSPD) and its output was sent into a lock-in amplifier (SR844, Stanford Research Systems). The lock-in reference was at the difference frequency of the two trigger signals (QCL and function generator), which was generated through an electrical frequency mixer and band pass filter. By recording the lock-in output as a function of QCL wavelength, the sample photoexpansion spectrum was obtained with heterodyne detection. The sample was 300 nm-thick poly(methyl methacrylate) (PMMA) patterned in the Texas-Longhorn shape (by e-beam lithography) on top of a 200 nm-thick uniform LOR film.

The cantilever had the second bending mode at ~200 kHz. In order to have the heterodyne signal amplified by this mode, we set the tip oscillation frequency ω_p at ~800 kHz and the laser pulse repetition frequency ω_l at ~600 kHz. Fine-tuning of ω_p was performed to ensure the difference frequency $\omega_- = \omega_p - \omega_l$ exactly matches the cantilever second bending mode.

First, the generation of the heterodyne signal was verified in Fig. 6.3(a). We selectively turned on the laser and/or the tip oscillation, and recorded the corresponding cantilever response in the frequency domain. In this demonstration, the AFM tip was positioned on top of PMMA and the laser wavelength was moved to the carbonyl absorption peak at 1730 cm^{-1}. Figure 6.3(a) confirmed that the heterodyne signal could only be generated when the light induced sample photoexpanison was interacting with the tip oscillation in the short-distance region.

Figure 6.3(b,c) demonstrates the resonance enhancement by the cantilever second bending mode. We scanned one frequency (tip or laser pulse repetition frequency) while keeping the other fixed. In both cases, the lock-in signal got enhanced when the heterodyne force was repeated at the cantilever resonant frequency.

According to Eq. (6.4), the heterodyne force can be amplified by the tip oscillation Δz_{tip}. This was demonstrated in Fig. 6.3(d) where we increased Δz_{tip} from zero (by applying voltage to the bimorph piezo) and observed that at first the lock-in signal was increased linearly. However, since the nonlinear tip-sample interaction only

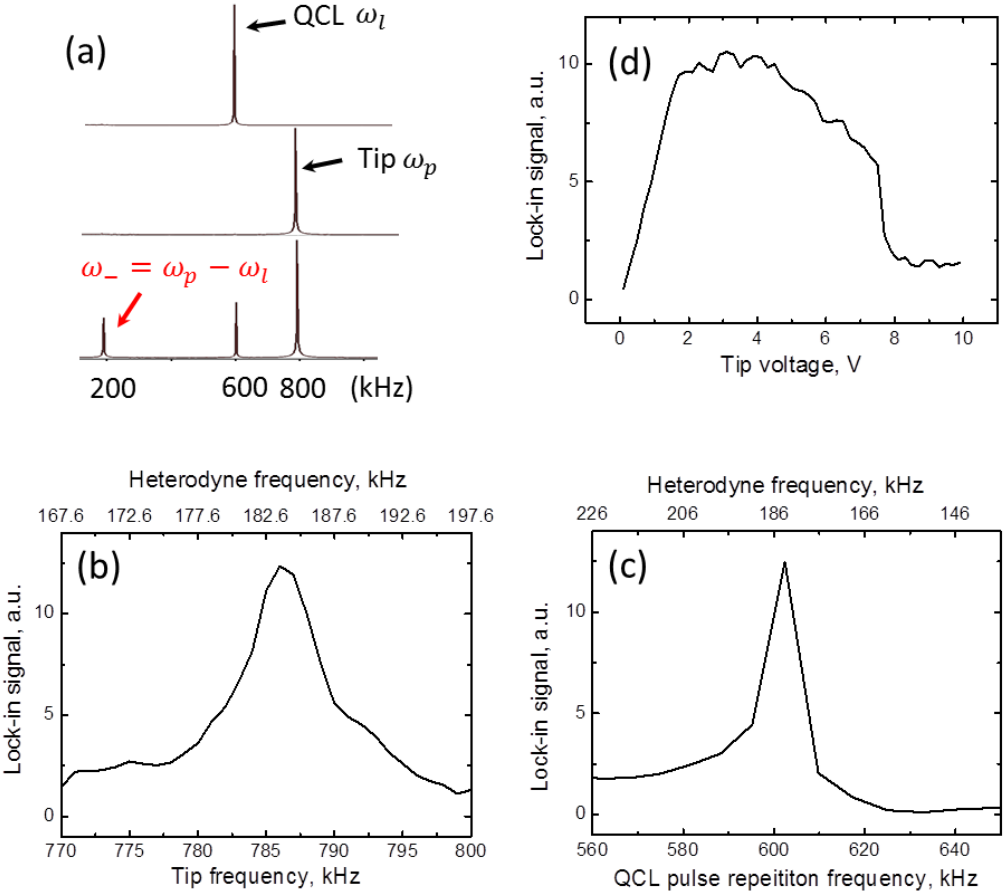

Figure 6.3: Heterodyne signal generation and amplification. **(a)** Recorded cantilever responses in three cases: (top) only the laser was on, (middle) only the tip was oscillated, (bottom) both the laser and the tip oscillation were activated. The data was recorded with a spectrum analyzer. The QCL wavelength was tuned to PMMA's carbonyl peak at 1730 cm^{-1}. **(b,c)** Recorded heterodyne signal as a function of (b) the tip oscillation frequency and (c) the laser pulse repetition frequency. **(d)** Recorded heterodyne signal as a function of tip oscillation amplitude.

happens near the sample surface (see Fig. 6.1), when Δz_{tip} was further increased, the lock-in signal was decreased.

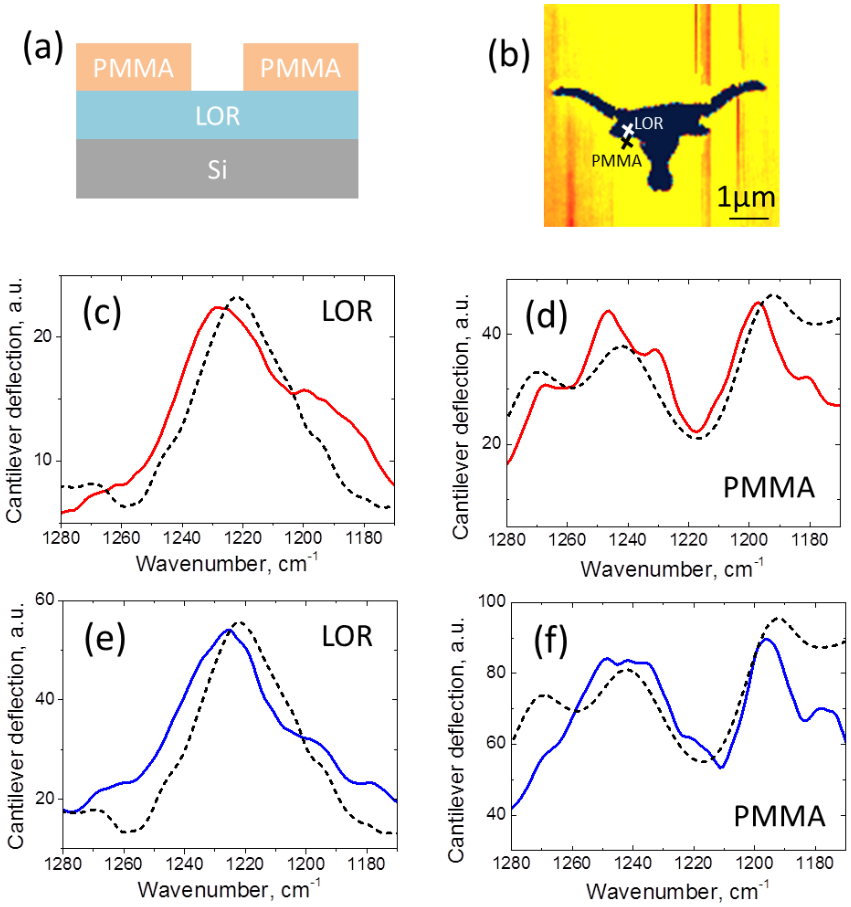

Figure 6.4: Heterodyne photoexpansion spectra with 100 nm spatial resolution. **(a)** Top view of the testing sample. **(b)** AFM topographic image **(c,d)** Heterodyne photoexpansion spectra (red curves) of LOR (c) and PMMA (d) taken at the two locations marked in (b) with 100 nm separation. QCL pulse repetition frequency was ~600 kHz and the tip oscillated at ~800 kHz. The lock-in was referenced at ~200 kHz. **(e,f)** Conventional photoexpansion spectra (blue curves) of LOR (e) and PMMA (f) taken at the same locations with QCL pulses repeated at ~200 kHz and without tip oscillation.

To verify that the heterodyne signal in Fig. 6.3 is useful for spectroscopy, we set the heterodyne frequency at the second bending mode of the cantilever, optimized the tip oscillation amplitude, tuned the laser emission wavelengths, and recorded the lock-in output as a function of wavelength to produce heterodyne photoexpansion spectra. The results are presented in Fig. 6.4. The AFM tip was positioned at two locations across the interface of LOR and PMMA with a separation of 100 nm. The corresponding photoexpansion spectra (Fig. 6.4 (c,d)) are in good agreement with the absorption spectra measured by FTIR (dashed curve). At the same sample locations, conventional photoexpansion spectra were also collected (Fig. 6.4(e,f)) by directly matching the repetition frequency of laser pulses to the second bending mode and using it as the reference frequency of the lock-in. The heterodyne spectral have similar signal-to-noise ratio with that of the conventional spectral. The signal amplitude is smaller, but not by much (only a factor of ~2).

6.4 CONCLUSION

We have demonstrated a new technique to acquire sample's photoexpansion spectra. It involves additional tip oscillation in contact mode. The spectral signal is extracted at the heterodyne frequency which is mixed by the frequencies of laser pulse repetition and tip oscillation due to the nonlinear tip-sample interaction. This new technique is promising for performing photoexpansion spectroscopy at a preferred cantilever resonant mode not accessible to the laser source.

Chapter 7

Characterization of Plasmonic Metasurface

7.1 INTRODUCTION

In the previous chapters, we focused on using photoexpansion spectroscopy to identify organic compounds. In this chapter, we show that this technique can also be applied to characterize plasmonic metasurfaces. Metasurfaces have been explored extensively in recent years. They manifest extraordinary capability to control light transmission and phase within a thin layer of engineered nanoantennas whose thickness is only a fraction of the operation wavelength, therefore they are promising to substitute those conventional bulky optical components like lens [59,60], filter [61,62], waveplate [63] and nonlinear mixer [64,65], to name a few. Previously, metasurfaces were characterized only in the far field via transmission or reflection measurement. New techniques which can directly visualize light-matter interaction in the near field on nanoscale are highly desired for better understanding and better designing metasurfaces.

The near-field properties of plasmonic nanoantennas include local optical energy distribution and associated ohmic heat dissipation. Currently, s-NSOM is the most successful technique to map nanoscale electric filed distribution in both amplitude and phase by employing optical interferometric measurement [11–14,66–69]. However, it cannot probe ohmic heating generated inside nanoantennas, which represents the main non-radiative loss mechanism of plasmonic metasurfaces.

With photoexpansion microscopy, both of these two optical properties can be mapped on the nanoscale [70]. To image local optical energy distribution, one can coat the metasurface with a thin layer of absorptive polymer, and observe cantilever deflection caused by the polymer expansion which is due to its absorption of the 'hot spot' energy. To image local ohmic heating in nanostructures, one can coat the metasurface with a thin layer of IR transparent polymer. In this case, polymer heating is produced entirely by ohmic dissipation in nanostructures. Using nanosecond light pulse excitation, the thermal diffusion length in the polymer is well below the critical dimension of metasurfaces; therefore polymer heating will be highly localized and reflect nanoscale optical properties. An alternative method of mapping ohmic heating is to directly observe cantilever deflection caused by the expansion of metal itself [71].

7.2 EXPERIMENT

The metasurface investigated in this work was designed and fabricated by Shvets group in the UT physics department. It features circular dichroism (CD) transmission in the mid-IR region. CD refers to different absorption of left-circularly polarized (LCP) and right-circularly polarized (RCP) light by the sample. In exists in chiral molecules (those cannot be superimposed with their mirror images) like DNA double helix and cholesteric type liquid crystal, but is only measureable for bulky samples. On a two-dimensional metasurface with plasmon resonance excited in nanoantennas, CD is quite strong and according to Ref. [72] it originates from different ohmic heating induced by different local field distribution.

The unit cell of the plasmonic metasurface is shown in Fig. 7.1(a), which consists of a vertical dipole antenna and a horizontal monopole antenna that is connected to a vertical plasmonic wire running across the entire metasurface. The nanoantennas are

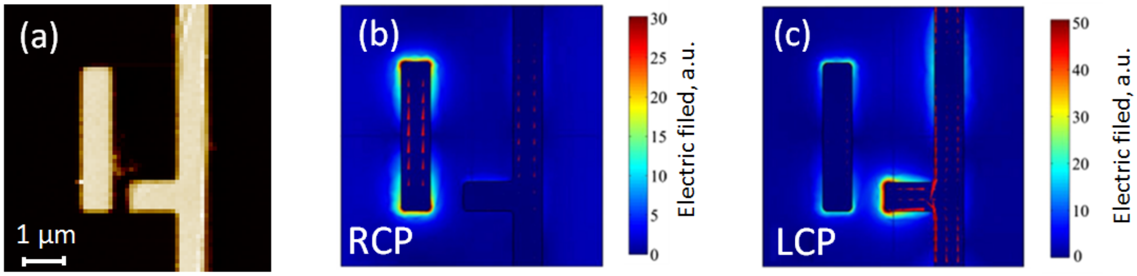

Figure 7.1: **(a)** AFM topography scanning of the chiral metasurface. **(b,c)** Surface current (arrows) and color-coded amplitude (left panel) of the normal electric field E_z from COMSOL simulations of normally incident RCP (b) and LCP (c) light waves.

made of 60-nm-thick gold on an IR transparent CaF2 substrate. Illuminating this metasurface with LCP/RCP light at the designed wavelength (λ ~ 9 µm) will excite different local filed distributions as simulated in Figs. 7.1(b,c), in which the strength of the red arrows is proportional to the induced current density (ohmic heating) in the nanoantennas.

The metasurface is designed to work at the resonance of the monopole antenna. A notable difference between Figs. 7.1(b) and 7.1(c) is that the monopole antenna is ‘turned on/off’ by LCP/RCP light. This is due to the constructive/destructive interference of two oscillating currents in the monopole antenna: one is induced by the excited vertical dipole antenna through the air gap, and the other is induced by the incident light itself.

To acquire the experimental evidence, we performed photoexpansion microscopy using the setup schematically shown in Figure 7.2. A pulsed mid-IR QCL (Daylight Solutions; tuning range 900–1200 cm^{-1}) operating at 9.1 µm wavelength was used to illuminate the sample from below at the normal incidence. The light from the QCL, originally linearly polarized, was converted to LCP or RCP light using an achromatic

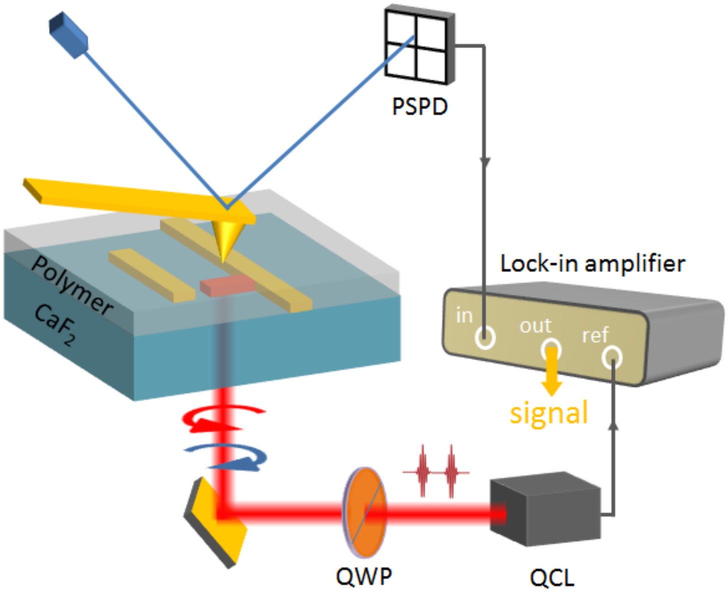

Figure 7.2: Schematic of experimental setup for mapping local optical energy distribution and ohmic heating on a chiral metasurface. The sample was illuminated by LCP/RCP light from a mid-IR QCL at normal incidence. QWP: quarter-wave plate.

quarter-wave plate (2-IRPW-ZO-L/4-8000-C, Altechna). The laser was operated with 200 ns pulses with the peak power of 300 mW at a repetition frequency of approximately 180 kHz, in resonance with the second bending mode of the AFM cantilever (ContGB-G, Budget Sensors). The beam was focused to a 100 μm-radius spot using ZnSe lens with the convergence half-angle of 4^o. The QCL pulse fluency on the sample surface is estimated to be approximately 1 kW cm^{-2}. The cantilever deflection was measured by a position-sensitive photodetector (PSPD) and its output was sent to a lock-in amplifier (SR844, Stanford Research Systems) using QCL pulse repetition frequency as a reference. The lock-in integration time was set at 10 ms. The output from the lock-in

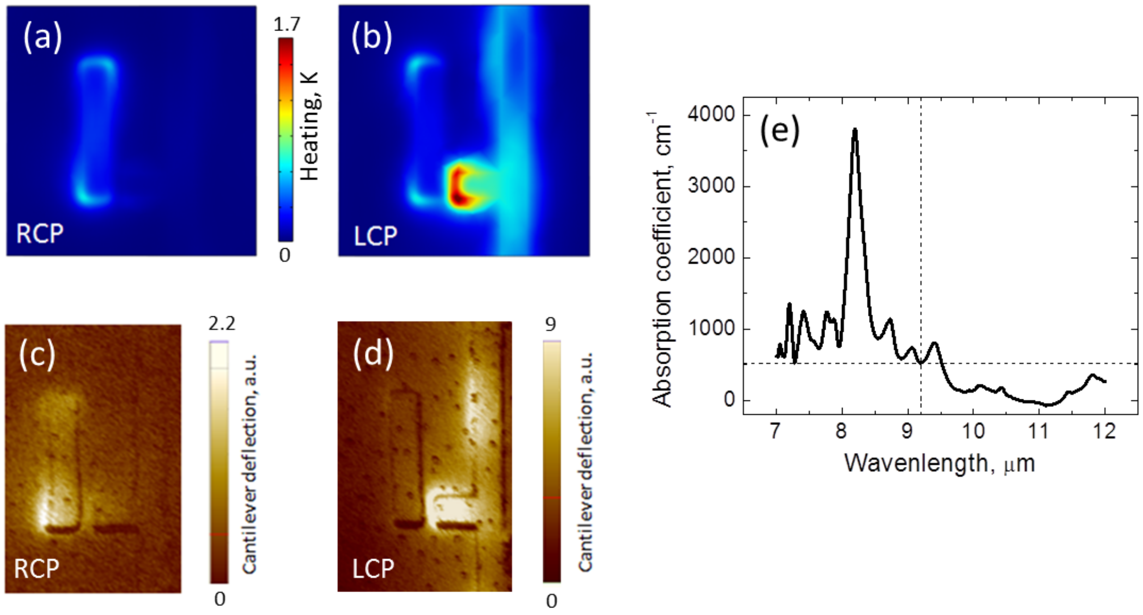

Figure 7.3: Photoexpansion microscopy measurements of circularly dichroic thermal expansion of the LOR-coated metasurface. **(a,b)** COMSOL simulations of the temperature increase distribution in the LOR film at the end of a square QCL pulse with time duration $T = 200$ ns and peak intensity $I = 1$kW cm^{-2} tuned to λ=9.1 μm, corresponding to the experimental conditions. **(c,d)** cantilever deflection on top of a LOR-coated sample excited with RCP (c) and LCP (d) laser pulses at normal incidence through the CaF_2 substrate. **(e)** Absorption spectrum of LOR polymer measured by FTIR.

amplifier was used to form images of 64 × 64 pixels by raster scanning the sample at a rate of 0.2 Hz.

First, the metasurface was spin-coated with a layer of 100-nm-thick LOR polymer, which has moderate absorption at the operation wavelength. In this case, the polymer heating and expansion was mainly produced by its absorption of locally enhanced optical energy around the nanoantennas induced by the incident light. As we can see from Figs. 7.1(b,c), under the LCP light illumination, the local optical energy is highest in the gap between two nanoantennas; while under the RCP light illumination, the highest local optical energy is outside the vertical dipole antenna. These nanoscale features are correctly reflected on the polymer heating distribution which are simulated in Figs. 7.3(a,b). Figures 7.3(c,d) show the experimentally measured AFM cantilever deflection amplitude at different areas of the sample. The cantilever deflection is directly proportional to temperature increase in the sample during the laser pulse. The experimental data is in excellent agreement with theoretical predictions shown in Figs. 7.3 (a,b). (Here, the two simulation figures share the same color bar, but the experimental images use different color bars). It is noted that in these images relatively high signal is also presented on top of the gold nanoantennas, which is due to the ohmic heat transfer. This mixed signal will disappear if the coating polymer is strongly absorptive.

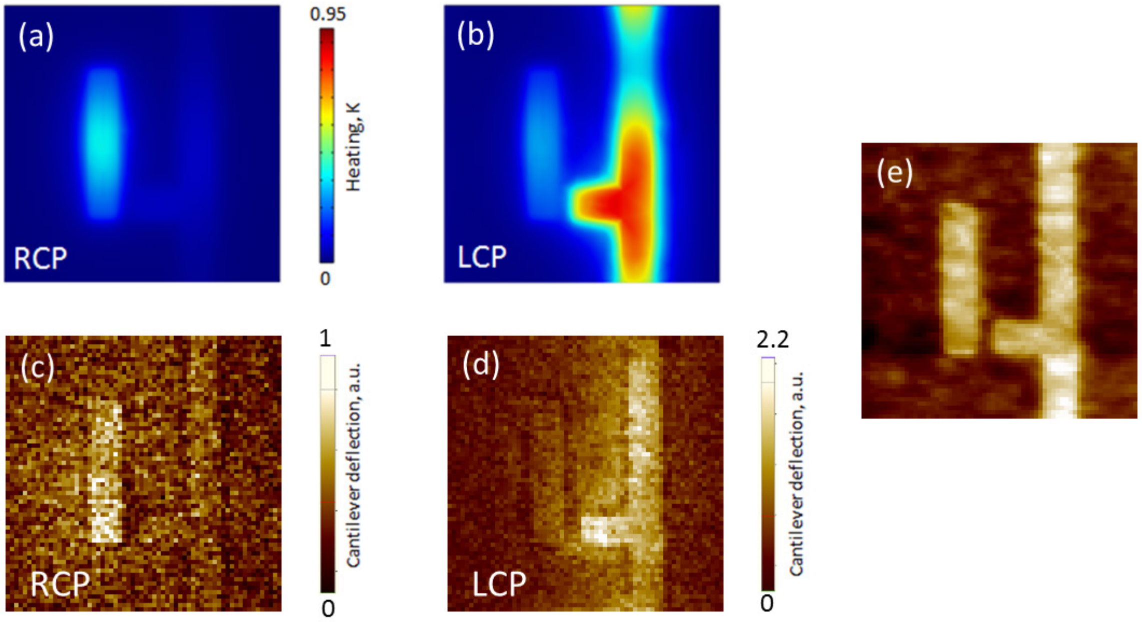

Figure 7.4: Photoexpansion microscopy measurements of circularly dichroic thermal expansion of the polyethylene-coated metasurface. **(a,b)** COMSOL simulations of the temperature increase distribution in the polyethylene film at the end of a square QCL pulse with time duration $T = 200$ ns and peak intensity $I = 1$kW cm^{-2} tuned to λ=9.1 μm, corresponding to the experimental conditions. **(c,d)** cantilever deflection on top of a polyethylene-coated sample excited with RCP (c) and LCP (d) laser pulses at normal incidence through the CaF_2 substrate. **(e)** AFM topography scanning of the polyethylene-coated metasurface.

Next, to map the pure local ohmic heat generation, we re-coated the metasurface with a layer of 100-nm-thick polyethylene via thermal evaporation. Polyethylene ($(CH_2)_n$) has simple chemical structure which makes it an effectively mid-IR transparent material: in the wavelength range of 5–10 μm, light absorption only happens at ~6.8 μm due to the C– H bending vibration.

With the polyethylene layer on top of the chiral metasurface, the polymer heating is produced entirely by the ohmic dissipation in the gold nanoantennas. Specifically, as predicted in Figs. 7.1(b,c), under the LCP light illumination, the ohmic heat (i.e. the current density) is dominantly generated in the monopole antenna; while under the RCP light illuminating, the ohmic heat is dominantly generated in the dipole antenna. These nanoscale features were correctly reflected on the polyethylene heating distribution with the simulation results presented in Figs. 7.4(a,b). Because the thermal diffusion length in polyethylene is well below 100 nm during the laser pulse, heating is found to be highly localized and to closely follow the distribution of ohmic dissipation in the gold nanoantennas. Figures 7.4(c,d) show the corresponding experimental data. It confirms that the magnitude and spatial distribution of the ohmic heating of a chiral two-dimensional metasurface dramatically depends on the handedness of light.

The local ohmic heat dissipation can also be imaged by observing the expansion of gold itself. The simulation results of gold heating distribution presented in Figs. 7.5(a,b) show that the temperature increase is up to ~1 K under the experimental conditions, which leads to gold expansion by ~0.8 pm. This is detectable in our setup. Figures 7.5(c,d) show the experimentally measured AFM cantilever deflection amplitude at different areas of the metasurface sample which has no polymer coating. In this case, the cantilever deflection is directly proportional to the temperature increase in gold during the laser pulse. The experimental data is in excellent agreement with the theoretical predictions shown in Figs. 7.5(a,b).

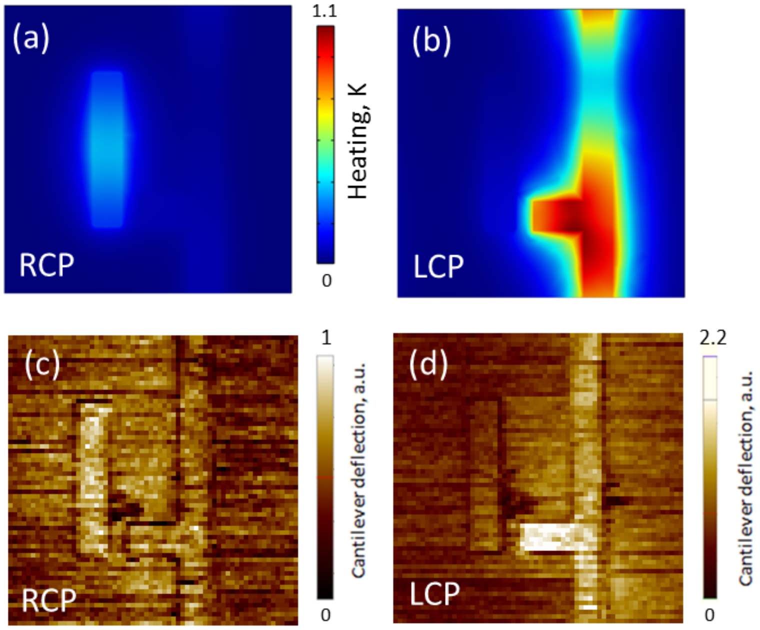

Figure 7.5: Photoexpansion microscopy measurements of circularly dichroic thermal expansion of the metasurface without polymer coating. **(a,b)** COMSOL simulations of the temperature increase distribution in the nanoantennas at the end of a square QCL pulse with time duration T = 200 ns and peak intensity I = 1kW cm^{-2} tuned to λ=9.1 μm, corresponding to the experimental conditions. **(c,d)** cantilever deflection on top of the metasurface excited with RCP (c) and LCP (d) laser pulses at normal incidence through the CaF$_2$ substrate.

7.3 CONCLUSION

We have demonstrated in this chapter that photoexpansion microscopy is a very versatile technique which is capable of imaging nanoscale optical energy distribution and ohmic heating of nanoantennas. This is facilitated by polymer coating on the device so that the local optical properties of nanoantennas are reflected on the heating and expansion of polymer. By far, photoexpansion microscopy is the only nanoscale tool to map local ohmic heating in metal nanoantennas.

Chapter 8

Conclusion

For the first time, monolayer sensitivity has been achieved in mid-IR photoexpanison nano-spectroscopy. The spectral signal is contributed by only ~300 molecules below the AFM cantilever tip. The cantilever in our experiments not only works as a force detector which has resonant response to the molecular expansion, but also works as an optical amplifier to generate locally enhanced field. The highly sensitive yet simple experimental configuration employs a compact sized and broadly tunable QCL as the mid-IR source. The spectroscopy technique we improved in this dissertation is readily applied to a variety of nano-samples in chemistry and biology.

In some cases, high spectral background is present due to the mid-IR absorption by the substrate and the AFM tip. We have demonstrated that the background signal can be removed from the lock-in detection by doubling its repetition frequency with additional substrate/tip heating and expansion induced by a second QCL.

Heterodyne detection of photoexpanison force has been explored. The obtained heterodyne spectra with signal amplified by the tip oscillation are of similar quality to the traditional photoexpanison spectra. This new frequency mixing technique is potentially useful for operating at a preferred cantilever resonant mode with a pulse repetition limited laser source.

Lastly, we have shown that photoexpansion microscopy can also be applied to image local optical energy distribution and ohmic heat dissipation of metal nanoantennas. This unique application makes our technique a versatile nanoscale tool for photonics research.

For the future, nanoscale characterization in the terahertz region (f = 1–10 THz) is particularly attracting. THz absorption spectroscopy can probe molecule's rotational modes [2] and give details about fine structures of chemicals. Photoexpansion measurement which does not rely on an external photodetector is readily extended to this spectral range, once tunable THz-QCLs with adequate output power are available.

Bibliography

1. Barbara H. Stuart. *Infrared Spectroscopy: Fundamentals and Applications*. (Wiley, 2004).

2. Wilson, E. B., Decius, J. C. & Cross, P. C. *Molecular Vibrations: The Theory of Infrared and Raman Vibrational Spectra*. (Dover Publications, 1955).

3. Born, M. & Wolf, E. *Principles of Optics*. (Cambridge University Press, 1997).

4. Zhang, W., Yeo, B. S., Schmid, T. & Zenobi, R. Single molecule tip-enhanced Raman spectroscopy with silver tips. *J. Phys. Chem. C* **111**, 1733–1738 (2007).

5. Neacsu, C., Dreyer, J., Behr, N. & Raschke, M. Scanning-probe Raman spectroscopy with single-molecule sensitivity. *Phys. Rev. B* **73**, 193406 (2006).

6. Steidtner, J. & Pettinger, B. Tip-enhanced Raman spectroscopy and microscopy on single dye molecules with 15 nm resolution. *Phys. Rev. Lett.* **100**, 236101 (2008).

7. Zhang, R. *et al.* Chemical mapping of a single molecule by plasmon-enhanced Raman scattering. *Nature* **498**, 82–86 (2013).

8. Pettinger, B., Schambach, P., Villagómez, C. J. & Scott, N. Tip-enhanced Raman spectroscopy: near-fields acting on a few molecules. *Annu. Rev. Phys. Chem.* **63**, 379–99 (2012).

9. Boyd, R. W. *Nonlinear Optics*. (Academic Press, 2008).

10. Moskovits, M. Surface-enhanced Raman spectroscopy: a brief retrospective. *J. Raman Spectrosc.* **36**, 485–496 (2005).

11. Hillenbrand, R., Taubner, T. & Keilmann, F. Phonon-enhanced light matter interaction at the nanometre scale. *Nature* **418**, 159–62 (2002).

12. Huth, F. *et al.* Nano-FTIR absorption spectroscopy of molecular fingerprints at 20 nm spatial resolution. *Nano Lett.* **12**, 3973–8 (2012).

13. Taubner, T., Hillenbrand, R. & Keilmann, F. Nanoscale polymer recognition by spectral signature in scattering infrared near-field microscopy. *Appl. Phys. Lett.* **85**, 5064 (2004).

14. Schnell, M. *et al.* Nanofocusing of mid-infrared energy with tapered transmission lines. *Nat. Photonics* **5**, 283–287 (2011).

15. Govyadinov, A. A., Amenabar, I., Huth, F., Carney, P. S. & Hillenbrand, R. Quantitative measurement of local infrared absorption and dielectric function with tip-enhanced near-field microscopy. *Phys. Chem. Lett.***4**, 1526–1531 (2013).

16. Dazzi, A., Prazeres, R., Glotin, F. & Ortega, J. M. Local infrared microspectroscopy with subwavelength spatial resolution with an atomic force microscope tip used as a photothermal sensor. *Opt. Lett.* **30**, 2388–90 (2005).

17. Lu, F. & Belkin, M. A. Infrared absorption nano-spectroscopy using sample photoexpansion induced by tunable quantum cascade lasers. *Opt. Express* **19**, 19942–7 (2011).

18. Lu, F., Jin, M. & Belkin, M. A. Tip-enhanced infrared nanospectroscopy via molecular expansion force detection. *Nat. Photonics* **8**, 307–312 (2014).

19. Katharina Von Puttkamer, Hans-Rolf Dubal, M. Q. Time-dependent processes in polyatomic molecules during and after intense infrared irradiation. *Faraday Discuss. Chem. Soc.* **75**, 197–210 (1983).

20. Mark, J. E. *Physical Properties of Polymers Handbook.* (Springer, 2007).

21. Derjaguin, B. V., Muller, V. M. & Toporov, Y. P. Effect of contact deformations on the adhesion of particles. *J. Colloid Interface Sci.* **53**, 314–326 (1975).

22. Israelachvili, J. N. *Intermolecular and Surface Forces*. (Elsevier, 2011).

23. Garcia, R. & Herruzo, E. T. The emergence of multifrequency force microscopy. *Nat. Nanotechnol.* **7**, 217–26 (2012).

24. Search, H., Journals, C., Contact, A., Iopscience, M. & Address, I. P. Calculation of thermal noise in atomic force microscopy. *Nanotechnology* **6**, 1–7 (1995).

25. Rabe, U., Janser, K. & Arnold, W. Vibrations of free and surface-coupled atomic force microscope cantilevers: Theory and experiment. *Rev. Sci. Instrum.* **67**, 3281 (1996).

26. Naeli, K. & Brand, O. Dimensional considerations in achieving large quality factors for resonant silicon cantilevers in air. *J. Appl. Phys.* **105**, 014908 (2009).

27. Landau, L. D. & Lifshitz, E. M. *Statistical Physics*. (Elsevier, 2013).

28. Anderson, M. S. Infrared spectroscopy with an atomic force microscope. *Appl. Spectrosc.* **54**, 349–352 (2000).

29. Lahiri, B., Holland, G. & Centrone, A. Chemical imaging beyond the diffraction limit: experimental validation of the PTIR technique. *Small* **9**, 439–45 (2013).

30. Kjoller, K., Felts, J. R., Cook, D., Prater, C. B. & King, W. P. High-sensitivity nanometer-scale infrared spectroscopy using a contact mode microcantilever with an internal resonator paddle. *Nanotechnology* **21**, 185705 (2010).

31. Felts, J. R. *et al.* Atomic force microscope infrared spectroscopy on 15 nm scale polymer nanostructures. *Rev. Sci. Instrum.* **84**, 023709 (2013).

32. Dazzi, a *et al.* Chemical mapping of the distribution of viruses into infected bacteria with a photothermal method. *Ultramicroscopy* **108**, 635–41 (2008).

33. We obtain sample temperature change in the range 5–50 K using the experimental parameters reported in Refs. [16], *Nanotechnology* **21**, 185705 (2010) and *Mater. Today* **13**, 56–60 (2010), and the simulation results reported in *Ultramicroscopy* **108**, 635–641 (2008).

34. Hida, H. *et al.* Fabrication of a quartz tuning-fork probe with a sharp tip for AFM systems. *Sensors Actuators A Phys.* **148**, 311–318 (2008).

35. Chen, G. Y., Warmack, R. J., Thundat, T., Allison, D. P. & Huang, A. Resonance response of scanning force microscopy cantilevers. *Rev. Sci. Instrum.* **65**, 2532 (1994).

36. Melcher, J., Hu, S. & Raman, A. Equivalent point-mass models of continuous atomic force microscope probes. *Appl. Phys. Lett.* **91,** 053101 (2007).

37. Jerome Faist, Federico Capasso, Deborah L. Sivco, Carlo Sirtori, Albert L. Hutchinson, A. Y. C. Quantum cascade laser. *Science* **264,** 553–556 (1994).

38. Hugi, A. *et al.* External cavity quantum cascade laser tunable from 7.6 to 11.4 μm. *Appl. Phys. Lett.* **95**, 061103 (2009).

39. Maulini, R., Mohan, A., Giovannini, M., Faist, J. & Gini, E. External cavity quantum-cascade laser tunable from 8.2 to 10.4 μm using a gain element with a heterogeneous cascade. *Appl. Phys. Lett.* **88**, 201113 (2006).

40. Hugi, A., Maulini, R. & Faist, J. External cavity quantum cascade laser. *Semicond. Sci. Technol.* **25**, 083001 (2010).

41. Huth, F. *et al.* Resonant antenna probes for tip-enhanced infrared near-field microscopy. *Nano Lett.* **13**, 1065 (2013).

42. Marshall, G. M., Bensebaa, F. & Dubowski, J. J. Observation of surface enhanced IR absorption coefficient in alkanethiol based self-assembled monolayers on GaAs(001). *J. Appl. Phys.* **105**, 094310 (2009).

43. Harder, P., Grunze, M., Dahint, R. & Heidelberg, D. Molecular conformation in oligo (ethylene glycol) -terminated self-assembled monolayers on gold and silver surfaces determines their ability to resist protein adsorption. *J. Phys. Chem. B* **5647**, 426–436 (1998).

44. Xia, Y. & Whitesides, G. M. Soft lithography. *Annu. Rev. Mater. Sci* . **28**, 153–184

(1998).

45. Rundqvist, J., Hoh, J. H. & Haviland, D. B. Poly(ethylene glycol) self-assembled monolayer island growth. *Langmuir* **21**, 2981–7 (2005).

46. Hegner, Ma., Wagner, P. & Semenza, G. Ultralarge atomically flat template-stripped Au surfaces for scanning probe microscopy. *Surf. Sci.* **291**, 39–46 (1993).

47. Belkin, M., Wang, Q. & Pflugl, C. High-temperature operation of terahertz quantum cascade laser sources. *Top. Quantum* **15**, 952–967 (2009).

48. Merklin, G. T., He, L. & Griffiths, P. R. Surface-enhanced infrared absorption spectrometry of p-nitrothiophenol and its disulfide. *Appl. Spectrosc.* **53**, 1448 (1999).

49. DelRio, F. W., Jaye, C., Fischer, D. a. & Cook, R. F. Elastic and adhesive properties of alkanethiol self-assembled monolayers on gold. *Appl. Phys. Lett.* **94**, 131909 (2009).

50. Kohlgraf-Owens, D. C., Sukhov, S. & Dogariu, A. Mapping the mechanical action of light. *Phys. Rev. A* **84**, 011807 (2011).

51. Ciraci, S., Tekman, E., Baratoff, A. & Batra, I. P. Theoretical study of short- and long-range forces and atom transfer in scanning force microscopy. *Phys. Rev. B* **46**, 10411–10422 (1992).

52. Kolosov, O. & Yamanaka, K. Nonlinear detection of ultrasonic vibrations in an atomic force microscope. *Jpn. J. Appl. Phys.* (1993).

53. Shekhawat, G. S. & Dravid, V. P. Nanoscale imaging of buried structures via scanning near-field ultrasound holography. *Science* **310**, 89–92 (2005).

54. Cantrell, S. A., Cantrell, J. H. & Lillehei, P. T. Nanoscale subsurface imaging via resonant difference-frequency atomic force ultrasonic microscopy. *J. Appl. Phys.* **101**, 114324 (2007).

55. Tetard, L. *et al.* Imaging nanoparticles in cells by nanomechanical holography. *Nat. Nanotechnol.* **3**, 501–5 (2008).

56. Tetard, L. *et al.* Virtual Resonance and Frequency Difference Generation by van der Waals Interaction. *Phys. Rev. Lett.* **106**, 180801 (2011).

57. Verbiest, G. J., Oosterkamp, T. H. & Rost, M. J. Cantilever dynamics in Heterodyne Force Microscopy. *Ultramicroscopy* **135**, 113–20 (2013).

58. Verbiest, G. J. & Rost, M. J. Beating beats mixing in heterodyne detection schemes. *Nat. Commun.* **6**, 6444 (2015).

59. Yu, N. *et al.* Light propagation with phase reflection and refraction. *Science* **334**, 333–337 (2011).

60. Fattal, D., Li, J., Peng, Z., Fiorentino, M. & Beausoleil, R. G. Flat dielectric grating reflectors with focusing abilities. *Nat. Photonics* **4**, 466–470 (2010).

61. Landy, N. I., Sajuyigbe, S., Mock, J. J., Smith, D. R. & Padilla, W. J. Perfect metamaterial absorber. *Phys. Rev. Lett.* **100**, 1–4 (2008).

62. Tung Bui, S. *et al.* Small-size metamaterial perfect absorber operating at low frequency. *Adv. Nat. Sci. Nanosci. Nanotechnol.* **5**, 045008 (2014).

63. Zhao, Y. & Alù, A. Manipulating light polarization with ultrathin plasmonic metasurfaces. *Phys. Rev. B - Condens. Matter Mater. Phys.* **84**, 1–6 (2011).

64. Lee, J. *et al.* Giant nonlinear response from plasmonic metasurfaces coupled to intersubband transitions. *Nature* **511**, 65–9 (2014).

65. Wolf, O. *et al.* Phased-array sources based on nonlinear metamaterial nanocavities. *Nat. Commun.* **6**, 7667 (2015).

66. Schnell, M. *et al.* Controlling the near-field oscillations of loaded plasmonic nanoantennas. *Nat. Photonics* **3**, 287–291 (2009).

67. Yoxall, E., Schnell, M., Mastel, S. & Hillenbrand, R. Magnitude and phase-resolved infrared vibrational nanospectroscopy with a swept quantum cascade laser. **16**, 20295–20305 (2015).

68. Alonso-Gonzalez, P. *et al.* Real-space mapping of Fano interference in plasmonic metamolecules. *Nano Lett.* **11**, 3922–3926 (2011).

69. Alonso-González, P. *et al.* Resolving the electromagnetic mechanism of surface-enhanced light scattering at single hot spots. *Nat. Commun.* **3**, 684 (2012).

70. Lahiri, B., Holland, G., Aksyuk, V. & Centrone, A. Nanoscale imaging of plasmonic hot spots and dark modes with the photothermal-induced resonance Technique. *Nano Lett.* **13**, 3218–3224 (2013).

71. Katzenmeyer, A. M. *et al.* Nanoscale imaging and spectroscopy of plasmonic modes with the PTIR technique. *Adv. Opt. Mater.* **2**, 718–722 (2014).

72. Khanikaev, A. B. *et al.* Experimental demonstration of the microscopic origin of circular dichroism in two-dimensional metamaterials. *Nat. Commun.* under review (2015).